REPORT DOCUMENTATION PAGE

Form Approved
OMB No. 0704-0188

The public reporting burden for this collection of information is estimated to average 1 hour per response, including the time for reviewing instructions, searching existing data sources, gathering and maintaining the data needed, and completing and reviewing the collection of information. Send comments regarding this burden estimate or any other aspect of this collection of information, including suggestions for reducing the burden, to Department of Defense, Washington Headquarters Services, Directorate for Information Operations and Reports (0704-0188), 1215 Jefferson Davis Highway, Suite 1204, Arlington, VA 22202-4302. Respondents should be aware that notwithstanding any other provision of law, no person shall be subject to any penalty for failing to comply with a collection of information if it does not display a currently valid OMB control number.
PLEASE DO NOT RETURN YOUR FORM TO THE ABOVE ADDRESS.

1. REPORT DATE *(DD-MM-YYYY)*	2. REPORT TYPE	3. DATES COVERED *(From - To)*
14-06-2007	Final	January 2003 - December 2006

4. TITLE AND SUBTITLE
A Vaporizing Liquid-Metal Anode for High-power Hall Thrusters

5a. CONTRACT NUMBER

5b. GRANT NUMBER
F49620-03-1-0027

5c. PROGRAM ELEMENT NUMBER

6. AUTHOR(S)
King, Lyon B.
Massey, Dean R.
Kieckhafer, Alex W.
Makela, Jason M.

5d. PROJECT NUMBER

5e. TASK NUMBER

5f. WORK UNIT NUMBER

7. PERFORMING ORGANIZATION NAME(S) AND ADDRESS(ES)
Michigan Technological University
1400 Townsend Drive
Houghton, MI 49931

8. PERFORMING ORGANIZATION REPORT NUMBER

9. SPONSORING/MONITORING AGENCY NAME(S) AND ADDRESS(ES)
AFOSR
1015 Wilson Blvd. Room 713
Arlington, VA 22203-1954
Dr Mitat Birkan/NA

10. SPONSOR/MONITOR'S ACRONYM(S)

11. SPONSOR/MONITOR'S REPORT NUMBER(S)
AFRL-SR-AR-TR-07-0207

12. DISTRIBUTION/AVAILABILITY STATEMENT
Approved for public release,
distribution unlimited

13. SUPPLEMENTARY NOTES

14. ABSTRACT

This report summarizes major findings from a three-year effort to develop and characterize a 2-kW bismuth Hall thruster. The device utilizes a set of segmented anodes, wherein discharge current can be shifted to control the temperature of a bismuth evaporator. Thruster performance on Xe is reported to establish a baseline attributable to segmented anode geometry separate from propellant species. Results are presented on bismuth, confirming the ability to maintain a self-sustaining metal-vapor plasma discharge using only waste heat from the thruster. Thermal failure of stainless-steel porous propellant diffusers is documented along with a fabrication strategy to construct diffusers using porous molybdenum. Results are presented for current and voltage behavior of a LaB6 cathode operating on bismuth vapors.

15. SUBJECT TERMS

16. SECURITY CLASSIFICATION OF:			17. LIMITATION OF ABSTRACT	18. NUMBER OF PAGES	19a. NAME OF RESPONSIBLE PERSON
a. REPORT	b. ABSTRACT	c. THIS PAGE			19b. TELEPHONE NUMBER *(Include area code)*

Final contract report for

AFOSR Grant Award No. F49620-03-1-0027

submitted to

Dr. Mitat Birkan
Government Program Manager
AFOSR/NA

Project Title

A Vaporizing Liquid-Metal Anode for High-Power Hall Thrusters

by

Lyon B. King
Associate Professor

Dean R. Massey
Alex W. Kieckhafer
Jason M. Makela

Mechanical Engineering – Engineering Mechanics
Michigan Technological University
815 RL Smith Bldg.
1400 Townsend Drive
Houghton, MI 49931
lbking@mtu.edu
(906) 487-2683

TABLE OF CONTENTS

1. Bismuth Hall Thrusters: A Propellant Comparison ____ *7*

1.1. Nomenclature ____ **7**

1.2. Introduction ____ **8**

1.3. Analysis of Propellants ____ **9**

1.4. Energetics of Propellants ____ **10**

1.4.1. Acceleration Kinetics ____ 10

1.4.2. Collision Considerations ____ 13

1.5. Analysis of Spacecraft Interactions for Bi, Xe, and Kr ____ **15**

1.6. Feed System for Condensible Propellant Operation ____ **17**

1.7. Conclusions ____ **18**

2. Description of Concept and Apparatus ____ *21*

2.1. Direct Evaporation ____ **21**

2.2. The Segmented Anode Hall Thruster ____ **22**

3. Segmented-Anode Thruster Performance: Xenon ____ *27*

3.1. Motivation for Xe Testing ____ **27**

3.2. Xe Test Facility and Apparatus ____ **27**

3.2.1. Vacuum Facility and Test Bed ____ 27

3.2.2. Performance Measurements ____ 28

3.2.3. Faraday Probe ____ 29

3.2.4. Retarding Potential Analyzer ____ 29

3.2.5. Emissive Probe ____ 30

3.2.6. ExB Probe ____ 30

3.3. Results ____ **32**

3.3.1. Thermal Performance ____ 32

3.3.2. Thrust Performance ____ 32

3.3.3. Plume Divergence ____ 38

3.3.4. Ion Energy Characterization ____ 41

3.3.5. Multiply Charged Ion Fraction ____ 43

3.4. Discussion ____ **46**

3.4.1. Thermal Data ____ 46

3.4.2. Performance Changes ____ 46

3.4.3. Plume Changes ____ 48

3.4.4. Efficiency Analysis ____ 49

3.5. Conclusions ____ **50**

4. Bismuth Thruster Operation ____ *54*

4.1. Initial Results using Xe Hot Start ____ **54**

4.2. Resistively Heated Vaporizer Design ____ **56**

4.3. Porous Vaporizer Performance ____ **59**

4.4. Thermal Failure of the Stainless-Steel Vaporizer ____ **63**

4.5. Porous Molybdenum Vaporizer 64

4.6. Conclusions 68

5. Bismuth Cathode Development *69*

5.1. Nomenclature 69

5.2. Introduction 69

5.3. Description of Apparatus 69

5.4. Results 70

5.4.1. Bismuth Operation 71

5.4.2. Comparison with Xenon and Krypton 72

5.5. Discussion 73

5.5.1. Required Heater Power 73

5.5.2. I-V Characteristics 73

5.5.3. Mass flow analysis 74

5.6. Conclusions 75

TABLE OF FIGURES

Figure 1-1. Change in thrust as a function of propellant ion mass, assuming constant acceleration voltage. 11
Figure 1-2. Fraction of thruster power required for ionization vs. I_{sp} for all propellants examined. 12
Figure 1-3. Electron-Impact Ionization Cross Sections for bismuth[26], cesium[27], iodine[28], krypton[30], mercury[31], and xenon[30] between threshold and 200 eV. 13
Figure 1-4, Sputter Yield of carbon under bismuth, xenon and krypton ion collisions. 16
Figure 1-5. Erosion Rate of Carbon per kilogram of bismuth, xenon, and krypton ions. 17
Figure 2-1. System power for an externally heated bismuth supply system. 21
Figure 2-2. MTU-patented energy harvesting scheme to use plasma discharge waste heat from electron attachment to the anode for bismuth evaporation. 22
Figure 2-3. Cross section of segmented-anode thruster for direct evaporation of bismuth. The shim electrodes can be used to intercept a fraction of the discharge current and, hence, control the heat deposition to the main anode/bismuth reservoir. 23
Figure 2-4. Electrical schematic of thruster test apparatus. Numbered annotations are 1: xenon propellant flow (for test with Xe instead of Bi), 2: shim power supply, 3: main anode power supply, 4: outer shim electrode, 5: main anode and gas distributor, 6: inner shim electrode, 7: cathode, 8: anode thermocouple, 9: inner shim thermocouple, and 10: outer shim thermocouple. 23
Figure 2-5. Calculated Bi evaporation rate as a function of temperature. 24
Figure 2-6. Thermal simulation of segmented anode thruster. In the top figure, 100% of the discharge current is attached to the main anode. In the bottom, all of the current is intercepted by the inner shim electrode. 25
Figure 2-7. Photograph of segmented-anode Hall thruster based on the Aerojet BPT-2000. 26
Figure 3-1. Top view of Xe test facility. 28
Figure 3-2. Thruster mounted on thrust stand in Xe test facility at the Isp Lab. 28
Figure 3-3. Thermal response of the segmented-anode Hall thruster with 400 V on the main anode. Temperature uncertainty is approximately 1%. 32
Figure 3-4: Characteristic shift in current on the shims and main anode as shim voltage was varied. Thruster was operating at 350 V on the anode and 5 mg/s of mass flow. 33
Figure 3-5: Thrust measured as a function of all three experimental factors. Higher shim voltages for a given mass flow and anode voltage combination correspond to higher discharge heating acceptance by the shims. 34
Figure 3-6: Specific Impulse as a function of shim voltage for all thruster operating conditions tested. Higher shim voltage for a given anode voltage indicates higher discharge electron heating on the shims. 35
Figure 3-7:Thruster Efficiency as a function of all three experimental factors. Higher shim voltage for a given anode voltage indicates higher discharge heating on the shims. 36
Figure 3-8: Beam Profiles with 350 V on the anode at all mass flows and levels of discharge current heating. 39
Figure 3-9: Beam divergence as a function of all three experimental factors. 40
Figure 3-10: Derivatives of RPA current with at 4 mg/s of xenon, at all combinations of anode voltages and shim levels. 42
Figure 3-11: Most Probable Ion Energy as a function of all three experimental factors. Higher shim voltage indicates a higher proportion of discharge current on the shims. 43
Figure 3-12: typical set of ExB probe traces taken as the level of shim current was varied. Data are for 400 V on the anode and 4 mg/s of xenon. 44

Figure 3-13: Average ion charge as a function of all three experimental factors. High shim voltage for indicates a higher fraction of discharge current heating on the shims. 45
Figure 4-1. Dual-propellant anode cross section. Porous phase descriminator was constructed from stainless-steel. 54
Figure 4-2. Current, power, and Xe flow rate during a "jump start" from Xe to Bi operation. 55
Figure 4-3. Balance of forces in response to a non-wetting fluid interacting with a capillary. 56
Figure 4-4. Bismuth wetting tests on stainless steel (A), molybdenum (B) and tungsten (C) substrates. In all cases the contact angle exceeds 90 therefore bismuth is non-wetting on these materials. 56
Figure 4-5. Model of liquid bismuth-porous plate interface with electron heating. Surface tension prevents the liquid from flowing through the pore yet gives a free surface for evaporation..57
Figure 4-6. Extrusion test set-up (left). Electron micrograph of a 10-mm commercially sintered stainless-steel plate showing the statistical variation of pore size (right). 58
Figure 4-7. Photo of an anode laying vaporizer-side up. 59
Figure 4-8. Photograph showing 2-kW bismuth thruster operating. 60
Figure 4-9 – Plot of a typical extended duration testing. After the initial warm up and transient period, steady state operation ensues. 60
Figure 4-10 – I-V characteristics for typical HET at different mass flow rates illustrating how discharge voltage compensates for varying mass flows. 61
Figure 4-11 – RPA data taken at 500 mm down stream of the thruster exit plane on centerline. The expected energy of the exhausted ions is approximately 360 volts. 62
Figure 4-12 – Faraday probe sweep of the exhaust plume taken at 250 mm showing a focused beam. 62
Figure 4-13 – Thermal image of the thruster taken immediately after an extended duration test. Vaporizer face temperature is uniform and the magnetic circuit is below the Curie point. ...63
Figure 4-14 – Vaporizer during the early stages of bismuth intrusion into the discharge chamber. 64
Figure 4-15 – FESEM micrograph at 600x showing some of the bulk features of the sintered molybdenum. This sample was sintered for 20 hours at 1100°C under high vacuum. 66
Figure 4-16 – FESEM micrograph of a representative sintered molybdenum disc at 1000x magnification. The apparent rough features of the sample indicates that late stage sintering is complete and grain growth of individual particles has occurred. This sample was sintered for 20 hours at 1100°C under high vacuum. 66
Figure 4-17 - FESEM micrograph of a representative sintered molybdenum disc at 40,000x magnification. The inter-particle grain boundaries are almost indistinguishable from the grains grown on the individual particles. This sample was sintered for 20 hours at 1100°C under high vacuum. 67
Figure 4-18 – Completed porous molybdenum vaporizer faces ready for electron beam welding. 67
Figure 5-1. Bismuth cathode schematic and thermocouple placement. 70
Figure 5-2. Operating bismuth cathode (top) and electrical schematic (bottom). 71
Figure 5-3. Temperature data taken near the bismuth reservoir, the cathode center, and the end orifice by thermocouples 1, 2, and 3, respectively, throughout the duration of the bismuth cathode test. 72
Figure 5-4. Anode voltage taken at currents varying from 2 to 16 Amps at a mass flow rate of 0.71 mg/s using bismuth. 72
Figure 5-5. Anode voltage taken at currents varying from 2 to 16 amps using krypton and xenon propellants. 73
Figure 5-6. Bismuth evaporation rate per surface area as a function of temperature. 74

TABLE OF TABLES

Table 1-1: Physical properties of candidate propellants.....10
Table 1-2: Number of ionizing collisions experienced by propellant atoms in a 100-mm channel. 14
Table 1-3: First and Second Ionization Energies.....15
Table 3-1. Thruster operating conditions examined. 37
Table 4-1. Hydrostatic extrusion test results.....57

1. Bismuth Hall Thrusters: A Propellant Comparison

1.1. Nomenclature

E_i ..... Ion energy (eV)

E_{ion} ..... Ionization energy (J/kg)

E_{th} ..... Sputtering Threshold Energy (eV)

F ..... Thrust (N)

g ..... gravitational acceleration (9.8 m/s^2)

I_{sp} ..... Specific Impulse (s)

k ..... Boltzmann Constant (1.38×10^{-23} $m^2 kgs^{-2} K^{-1}$)

L ..... Discharge chamber length (m)

$\dot{m}$ ..... mass flow rate (kg/s)

M_i ..... Ion mass (kg)

M_n ..... Mass of species n (kg)

M_s ..... Atomic mass of surface material(kg)

M_{Xe} ..... Mass of a xenon atom (kg)

n_e ..... Electron density (m^{-3})

P_{ion} ..... Power required for propellant ionization (W)

P_{kin} ..... Exhaust kinetic power (W)

q_i ..... Ion charge (C)

Q_s ..... Surface sputtering parameter

$S_e(\varepsilon)$ ..... Reduced Lindhard electronic stopping cross section (m^2)

$S_n(\varepsilon)$ ..... Nuclear stopping cross section (m^2)

T ..... Temperature (K)

t_r ..... Residence time (s)

u_e ..... exhaust velocity (m/s)

$(u_e)_{Xe}$ ..... velocity of xenon (m/s)

U_0 ..... Surface binding energy (eV)

V_a ..... Effective acceleration voltage (V)

$\overline{v}_e$ ..... Average electron velocity (m/s)

$\overline{v}_n$ ..... Average neutral atom velocity (m/s)

Y_E ..... Sputter Yield (atoms/ion)

α_s ..... Surface sputtering parameter

γ ..... Elastic energy transfer factor

ε ..... Reduced energy parameter (eV)

ν ..... Ionizing collision frequency (Hz)

$\overline{\sigma}$ ..... Average electron-impact ionization cross section (m^2)

1.2. Introduction

An emerging hurdle in high-power Hall thruster development has been the use of xenon as the propellant of choice. While xenon has several advantages as a propellant, namely low ionization energy, high atomic mass and easy storage and flow metering, several disadvantages preclude the use of xenon in very high power thrusters. The first disadvantage to xenon as an Electric Propulsion (EP) propellant is its high cost. Currently xenon can be purchased for approximately $6.65 per standard liter ($1140/kg) in small quantities.[1] Using current commercial prices, a 500-kW Hall thruster operating at 60% anode efficiency and 2,000 s Specific Impulse (I_{sp}) will consume $6,400 of xenon per hour of operation. These costs can be extrapolated to $153,600 per test day, and $64M for a 10,000-hour mission. Longer-duration missions utilizing larger thrusters or many smaller thrusters can quickly become relatively expensive to supply with propellant. To reduce this cost, more economical propellants need to be utilized. Studies have focused on krypton as a more-economical alternative to xenon, while maintaining the general design of a gas-propelled thruster.[2]

The second major disadvantage to xenon is in ground testing. Thruster exhaust must be evacuated from a test facility in order to maintain a space-like vacuum. Typically, this is accomplished with cryogenic vacuum pumps. High facility pressures will affect the thruster performance and beam characteristics through an increase in charge-exchange ions created by collisions between exhaust ions and neutral atoms that remain the vacuum chamber. For a 500-

kW thruster operating at 2,000 s I_{sp} and 60% efficiency, 1.6 g/s of xenon will enter the chamber. In order to maintain a pressure of $1x10^{-5}$ Torr ($6.7x10^{-4}$ Pa) of xenon, the facility vacuum pumps must be capable of nearly 20M liters-per-second of pumping throughput. The pressure chosen was previously determined by Randolph to be sufficient to nearly eliminate facility backpressure effects. More recent observations[3] have shown this not to be entirely accurate, however for lack of another estimate of facility pressure, the estimate of Randolph will be used. At a cost of roughly $1 per-l/s,[4] this translates to roughly $20M in pumping equipment. The pumping requirements scale linearly with thruster power, so a 1-MW thruster will require nearly $40M in pumping equipment. Additional costs include the large vacuum chamber, support infrastructure and recurring costs such as liquid nitrogen. Unlike propellant costs, facility costs cannot be reduced unless gaseous propellant usage is eliminated, as any gaseous propellant will require evacuation from the facility.

Condensible propellants, defined as those species existing in either solid or liquid state at Standard Temperature and Pressure (0 °C, one atmosphere pressure) (STP) offer significant advantages for facility cost. While xenon, krypton, and other gaseous propellants must be actively evacuated from the test chamber, condensible propellants will naturally condense on the chamber walls, requiring no pumping. Thus, condensible propellants are 'self-pumping,' requiring only enough vacuum pump capacity to reach and maintain high vacuum with little to no gas load. Condensible propellants may also cost less than xenon or krypton, reducing testing costs further. Vacuum facility contamination may be an issue with condensable propellants, however. The coating of interior surfaces with propellant may require special handling procedures, especially for toxic and reactive propellants.

1.3. Analysis of Propellants

Many factors contribute to the suitability of a Hall thruster propellant. Factors that affect performance include ionization energy, atomic mass, and ease of mass flow system construction. Condensible propellants offer a challenge in mass flow systems, as traditional gas-fed systems utilized on xenon and krypton thrusters cannot be used. Generally, the higher the melting and boiling points of a propellant, the harder it will be to design and fabricate a mass flow system. Propellant ionization is another source of inefficiency. As energy spent on ionization is not available for acceleration, reduction of ionization energy will directly increase the efficiency of a thruster. Several practical issues also contribute to the suitability of a candidate propellant. These include cost, toxicity/reactivity, and potential for spacecraft contamination. Reducing propellant cost is of obvious benefit, as less-expensive propellants allow for reduced testing and mission costs. Several alternative propellant options have been considered.[5,6,7,8,9,10] Some physical properties of these propellants, including xenon as a point of comparison, are in Table 1-1. This section will discuss the relative merits and difficulties with the many propellant alternatives.

Several of the Hall thruster propellants considered are toxic and/or reactive. These include cadmium,[11] cesium,[12] iodine,[13] and mercury.[14] While each of these propellants offer lower propellant costs and ionization energy than xenon, they all present problems in a testing environment. Of these, iodine and cesium present significant reactivity hazards, while each presents a significant chronic and/or acute toxicity hazard. Currently there are no active development efforts on these propellants.

Table 1-1: Physical properties of candidate propellants

Propellant	Melting Point (°C)	Boiling Point (°C)	First Ionization Energy (eV)	Atomic Mass (amu)	Cost Per Kg
Bismuth (Bi)	271	1559	7.3	209.0	$6[15]
Cadmium (Cd)	321	765	9.0	112.4	$25[16]
Cesium (Cs)	29	685	3.9	132.9	$40,000[17]
Iodine (I)	113	182	10.4	126.9	$484[18]
Krypton (Kr)	-157	-153	14.0	83.8	$295[19]
Mercury (Hg)	-39	357	10.4	200.6	$4[20]
Xenon (Xe)	-112	-108	12.1	131.3	$1138[1]

Three of the propellants considered are relatively non-toxic and non-reactive. Xenon and krypton present essentially no toxicity threat except through displacement of oxygen.[21,22] Reactivity is also of little concern, as krypton will not spontaneously react with any substance, and xenon will react only with fluorine. Bismuth presents little hazard. It is considered mildly toxic and safety precautions involve exposure limitation only.[23] While conversion of a Hall thruster from xenon to krypton requires trivial redesign of the mass flow system, bismuth presents significant development issues due to its condensable nature. Bismuth thruster development is under consideration at Stanford/Jet Propulsion Laboratory (JPL) under the Very High Impulse Thruster with an Anode Layer (VHITAL) program,[24] Busek, Michigan Technological University[25], and Aerophysics, Inc.

1.4. Energetics of Propellants

1.4.1. Acceleration Kinetics

The most obvious disparity between propellant performance characteristics is a change in thrust under identical discharge voltage due to the different atomic mass. The mass ratio of the propellants is defined as:

$$MR = \frac{M_n}{M_{Xe}} \tag{1-1}$$

where MR is the mass ratio of the propellant to xenon. The thrust produced by a thruster is defined as $F = u_e \dot{m}$. Assuming that ions of any species are accelerated through the same voltage, the exhaust velocity will be:

$$u_e = \sqrt{\frac{2q_i V_a}{M_{xe}}}\sqrt{\frac{1}{MR}} = (u_e)_{Xe}\sqrt{\frac{1}{MR}} \tag{1-2}$$

and the thrust force is:

$$F = (u_e)_{Xe}\dot{m}\sqrt{\frac{1}{MR}} \tag{1-3}$$

which is the thrust force of a xenon thruster divided by the square root of the mass ratio. Mass flows may either be the same between different propellants, or they may be adjusted so the same number of moles of propellant are utilized per second. In the case where mass flow is constant, $\dot{m}$ will be the same for all propellant options. In the case where molar flow is constant, the mass flow will change according to MR, while the discharge current will remain approximately constant. If the mass ratio is adjusted so molar flow rate and thus thruster current is constant, then the thrust will be the thrust of a xenon thruster multiplied by the square root of the mass ratio. The trends in thrust for different propellant ion masses are plotted in Figure 1-1. I_{sp} under constant discharge voltage will be modified similarly to exhaust velocity. As I_{sp} is given by the equation:

$$I_{sp} = \frac{u_e}{g} \qquad 1\text{-}4$$

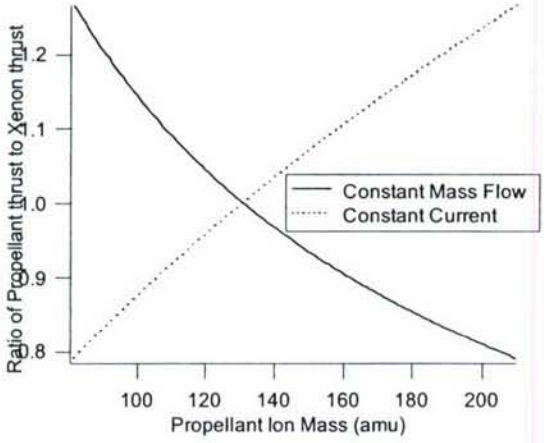


Figure 1-1. Change in thrust as a function of propellant ion mass, assuming constant acceleration voltage.

I_{sp} for any propellant is equal to the value for a xenon thruster, divided by the square root of the mass ratio. So a thruster that would normally operate on xenon at 2,000 s I_{sp} would operate on krypton at 2,500 s, and on bismuth at 1,583 s for the same discharge voltage, with the other propellant options falling between the krypton and bismuth specific impulses. In order to maintain the same I_{sp} with different propellants, the discharge voltage would need to be modified. Large variations in the discharge voltage (outside the current SOA of 200-600V) cause complications in plasma acceleration physics that may preclude the use of heavy atoms at high I_{sp}, or light atoms at low I_{sp}.

Aside from the exhaust kinetics, the choice of propellant has a direct influence on thruster efficiency. Ionization production represents a fundamental source of inefficiency, since any energy spent in creating an ion from a neutral is not available for conversion to beam kinetic energy. As the ionization energy is exhibited as a direct power loss from the thruster, keeping the ionization energy at a minimum will increase thruster efficiency. While ionization energy is typically expressed as the energy required to singly ionize one neutral atom (eV/atom), a more convenient form for thruster analysis is the amount of energy required per-kilogram of mass flow. This factor, E_{ion}, then accounts for the difference in ionization potentials as well as the difference

in atomic masses of the candidate species, and can be calculated by dividing the ionization energy by the mass of an atom. E_{ion} can then be employed in the equation:

$$P_{ion} = \dot{m}E_{ion} \tag{1-5}$$

We can use P_{ion} to calculate the maximum theoretical efficiency of an acceleration process assuming that the only energy loss is propellant ionization. Expressing the kinetic power in the exhaust beam as

$$P_{kin} = \frac{1}{2}\dot{m}u_e^2 = \frac{\dot{m}g^2 I_{sp}^2}{2} \tag{1-6}$$

Combining Eqn 1-5 with Eqn 1-6 yields:

$$\frac{P_{ion}}{P_{kin}} = \frac{2E_{ion}}{g^2 I_{sp}^2} \tag{1-7}$$

Eqn 1-7 is then the theoretical minimum efficiency penalty required to singly ionize and accelerate the propellant as a function of I_{sp}. These ratios are plotted in Figure 1-2.

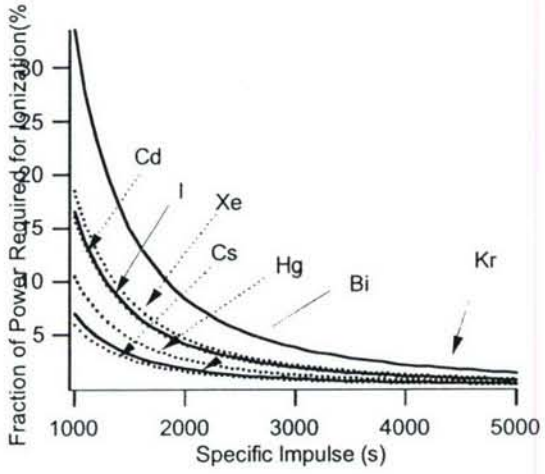


Figure 1-2. Fraction of thruster power required for ionization vs. I_{sp} for all propellants examined.

The propellants with lower ionization energy-per-mass (E_{ion}) require a smaller fraction of the total thruster power to ionize the propellant. It is also interesting to note that the difference between propellants becomes nearly insignificant at high I_{sp}. At 1,000 s, the fractions range from approximately 6% for cesium up to 34% for krypton, while at 5,000 s no propellant option requires significantly more than one percent of total thruster power (krypton is highest at 1.3%). It should be noted that these calculations are a theoretical minimum where all of the propellant is ionized, there are no doubly-charged ions, no energy is spent promoting atoms or ions to excited states, and all of the ions are produced only once; there is no wall recombination and re-ionization. Any re-ionization process will present an energy loss as an ion is essentially being created twice, requiring twice the energy expenditure. The ionization power will differ in a real thruster, however the relative scaling between propellants should remain similar.

1.4.2. Collision Considerations

Any neutral propellant that is not ionized within the discharge chamber prior to escaping the thruster internal volume represents inefficiency in propellant utilization (it is not electrostatically accelerated and contributes negligibly to thrust). The probability of ionization for a given atom subject to an electron collision is given by the ionization cross section. These cross sections are dependent on the energy of the impacting (ionizing) electron and the atomic structure of the propellant atom. Experimentally determined ionization cross-sections for bismuth[26], cesium[27,28], iodine[29], krypton[30], mercury[31], and xenon[30] were available in literature. Cross-section measurements for cadmium could not be found. A comparison of xenon with the other propellants is plotted in Figure 1-3.

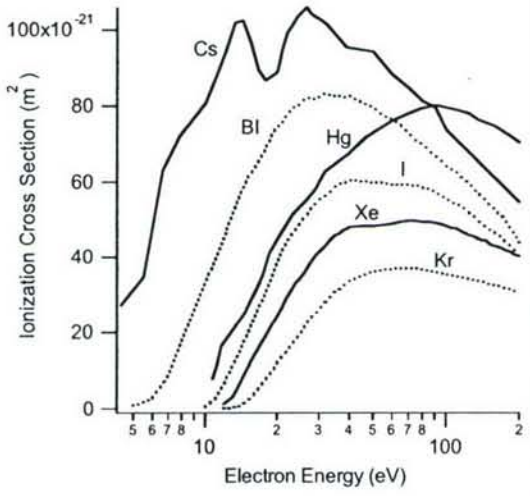


Figure 1-3. Electron-Impact Ionization Cross Sections for bismuth[26], cesium[27], iodine[28], krypton[30], mercury[31], and xenon[30] between threshold and 200 eV.

In general, the lower the atom's ionization energy the larger the ionization cross section. Thus cesium shows itself to be the most amenable to ionization, due to the extremely low ionization energy. However, bismuth and mercury do not have significantly lower cross sections than cesium. The smallest cross sections calculated were for the two propellants currently in use; xenon and krypton. Thus any change from xenon or krypton to another propellant discussed here will result in an increased probability of ionization within the discharge chamber.

Using the ionization cross-section, the rate of ionizing collisions can be calculated. The rate of ionizing collisions is given by:[32]

$$\nu = \bar{\sigma} n_e \sqrt{\bar{v}_n^2 + \bar{v}_e^2} \quad . \qquad 1\text{-}8$$

In order to calculate estimates of ν the electron velocity distribution function was calculated based on an assumed 20 eV temperature and the Maxwellian distribution.[33] The average electron-impact ionization cross section was calculated by integrating the product of the electron energy distribution function and the ionization cross section. $\bar{\sigma}$ is estimated assuming the propellant atoms are emitted with a thermal velocity distribution in equilibrium with the

anode/diffuser temperature. Average electron velocity is estimated similarly, assuming the temperature of the electrons is 20 eV. Given typical anode temperatures of 700 °C, the neutral velocity will be in the range of 300-500 m/s for all species. Since the average electron velocity is four orders of magnitude higher, the neutral velocity can be neglected. Thus, collision frequencies will scale simply with ionization cross-section and electron density. An electron number density of $2x10^{18}$ m^{-3} was measured by Haas and Gallimore in Ref. 33 and is used here as a representative value to calculate collision frequencies that may be typical within a Hall thruster discharge. Of critical importance to determination of the propellant utilization of a thruster is the electron temperature in the discharge channel. As it is impossible to determine the exact effect switching to another propellant will have on the electron temperature, values of electron temperature measured in xenon thrusters are used here for calculations. Calculated values of the collision frequency are in Table 1-2.

Table 1-2: Number of ionizing collisions experienced by propellant atoms in a 100-mm channel.

Propellant	Collision Frequency ($x10^5$ Hz)	Neutral Diffusion Velocity (m/s)	Number of Collisions
Bismuth	4.1	161	26
Cesium	5.5	202	32
Iodine	2.7	207	18
Krypton	1.4	254	6
Mercury	3.3	165	20
Xenon	2.1	203	10

While the trends in collision frequency among the propellant candidates simply mirror the cross section scaling of Figure 1-3, the magnitude of ν becomes particularly important in calculating the propellant utilization efficiency. In order to measurably contribute to the thrust, a propellant atom must be ionized before it is permitted to escape the discharge chamber. Thus if the residence time is defined as $t_r=L/v_n$ and v_n is defined as:

$$\bar{v}_n = \sqrt{\frac{kT}{2\pi m}} \qquad 1\text{-}9$$

The factor νt_r gives the ratio of residence time to collision time. Physically, this factor represents the average number of ionizing collisions experienced by a propellant atom before diffusing out of a discharge chamber of length L. If this factor is low, it is probable that propellant atoms will escape the discharge without being ionized. Using the calculated collision frequencies, assuming neutral atoms leave the gas diffuser with a temperature of 700°C, and assuming the neutral atoms must travel 100 mm to leave the channel, the average number of ionizing collisions for each propellant species is shown in Table 1-2.

While the gross simplification used in determining the number of collisions precludes any confidence in the absolute magnitude of the numbers, the relative trends between propellants is a reliable indicator of utilization. The calculated ionizing collision rates show significant differences between species. When compounded with the neutral diffusion velocity, some propellants show a much higher utilization than others. Krypton suffers here, as it has the lowest ionization cross section and the highest neutral diffusion velocity. Cesium, as expected, will experience the most ionizing collisions due to its very high ionization cross section. Of particular interest here, however, is bismuth, with an estimated number of collisions only slightly less than cesium. This is due in large part to the large cross section and extremely low neutral diffusion velocity of bismuth.

While it is important to have an electron population with enough energy to ionize the propellant, it is equally important not to have an electron population so energetic as to produce significant amounts of multiply-charged ions. Previous studies on xenon thrusters have given maximum electron temperatures above 15eV.[34,35] Probe-based studies of a 5-kW thruster at several operating points show the temperature is dependent on flow rate, and can be nearly 30eV in low mass-flow conditions.[33] Higher mass flows appear to cool the electrons, as the drifting electrons cannot acquire as much energy through 'falling' towards the thruster anode after a collision. Any population of electrons with temperature greater than the second ionization potential of the propellant may create multiply ionized propellant ions. Multiply charged ions represent an inefficient use of propulsive power. For instance, a doubly charged ion will contribute twice the discharge current (and hence, draw twice the power) as a singly charged ion, however will only be accelerated to a velocity $\sqrt{2}$ times more than its single counterpart.

Formation of multiply charged ions may be an issue for some propellants as shown in Table 1-3. Xenon has the drawback of a high first ionization energy, but its second ionization energy is quite high (21.2 eV); thus it does not readily produce Xe^{2+} in typical Hall thruster plasmas, with approximately 90% of the xenon ions singly charged.[36] Cesium and krypton also will not form large fractions of multiple ions. Other elements, such as bismuth and cadmium, may be sensitive to multiply charged ion efficiency losses in an electron population with temperatures similar to those seen in xenon devices.

Table 1-3: First and Second Ionization Energies

Propellant	First Ionization Energy (eV)	Second Ionization Energy (eV)
Bismuth	7.3	16.7
Cadmium	9.0	16.9
Cesium	3.9	23.2
Iodine	10.4	19.1
Krypton	14.0	24.4
Mercury	10.4	18.8
Xenon	12.1	21.2

1.5. Analysis of Spacecraft Interactions for Bi, Xe, and Kr

At this point, bismuth, xenon, and krypton will be chosen for further analysis. As bismuth is nearly as efficient as cesium, without the toxicity or reactivity drawbacks, it appears to be the best choice for a high-thrust, low-Isp thruster. Krypton is chosen as an alternative only for high-Isp operation, as it is too energetically costly to ionize to be useful in a low-Isp thruster.

The sputter rate of a propellant is highly important to thruster lifetime, especially at high Isp when propellant ions have significant energy. Typically, the maximum lifetime of the thruster is determined by the time required for sputter erosion to wear through the discharge channel walls and start eroding the electromagnet poles. The sputter yield of ions normally incident on a solid surface can be calculated by:[37]

$$Y(E) = 0.42 \frac{\alpha_s Q_s S_n(E)}{U_0 \left[1 + 0.35 U_0 S_e(\varepsilon)\right]} \left[1 - \sqrt{\frac{E_{th}}{E}}\right]^{2.8} \quad 1\text{-}10$$

Of particular interest is E_{th}, as sputtering does not occur when incident ions have energies below E_{th}. The sputtering threshold energy is calculated by:

$$E_{th} = \left(\frac{4}{3}\right)\frac{U_0}{\gamma} \qquad 1\text{-}12$$

where γ is the elastic energy transfer factor. This factor is involved in the calculation of the threshold sputtering energy, and thus affects the sputtering rate at all energies. γ is calculated by the equation:

$$\gamma = \frac{4M_i M_s}{(M_i + M_s)^2}. \qquad 1\text{-}12$$

Calculations were made for bismuth, krypton, and xenon ions incident on a carbon surface as a representative thruster material (it is unclear whether or how this model can be applied to BN as a target material). While carbon is not normally used in Hall thrusters, there has been experimental effort into using it as an electrode material.[38,39]

The sputtering threshold for ions on carbon was found to be different for each species; 202 eV for bismuth, 135 eV for xenon, and 95 eV for krypton. These results mean that for a given distribution of ion energies, fewer bismuth ions will be above the sputtering threshold than xenon or krypton. For ions above threshold, the model can be used to predict sputter rates. The calculated sputter rates over a range of ion energies are plotted in Figure 1-4.

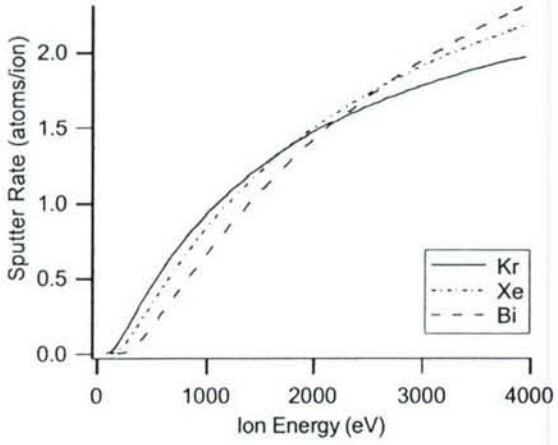


Figure 1-4, Sputter Yield of carbon under bismuth, xenon and krypton ion collisions.

The results of sputtering calculations show that bismuth will induce less sputtering on carbon substrates at energies anticipated in Hall thruster operation. At high energies (greater than 1,200 eV) bismuth will cause higher sputtering than xenon and krypton, however this range is beyond the operational envelope of SOA Hall thrusters. Bismuth's erosion advantage is further extended if sputtering is analyzed under constant mass flow. As bismuth has an atomic mass of 209 amu, nearly 60% greater than the atomic mass of xenon (131 amu) and 2.5 times as high as krypton (84 amu), a given mass flow of bismuth will contain fewer ions. To determine the effect of the increased mass of bismuth, the calculations were scaled to indicate the mass of surface sputtered away per unit mass of ions. These results are displayed in Figure 5 and show that bismuth will cause less erosion than xenon or krypton given equal mass flows. These results are encouraging for the lifetime of a bismuth thruster, as the thruster structures should exhibit lower erosion for the same total mass throughput. The erosion rate for bismuth remains less than xenon or krypton until the ion energies approach 10,000 eV, at which point the erosion rates converge.

For ion energies higher than 10,000 eV, which are not included in Figure 1-5, the lighter propellants become favorable. It should be noted that the erosion rate is primarily driven by the ion mass and atomic number, and the ratios of these to the atoms in the surface. As the other propellants analyzed fall between krypton and bismuth in size, they will exhibit sputter rates somewhere between those of krypton and bismuth.

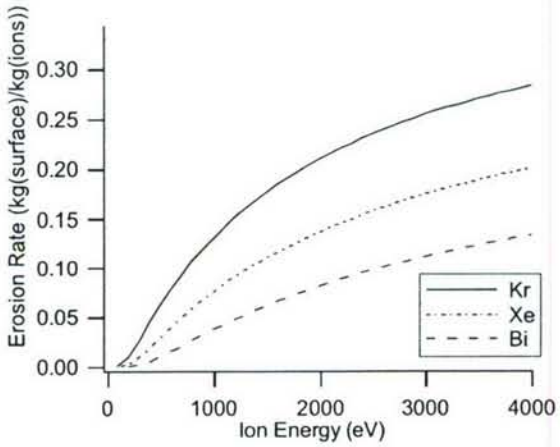


Figure 1-5. Erosion Rate of Carbon per kilogram of bismuth, xenon, and krypton ions.

One complicating factor for use of bismuth or any other condensable propellant is deposition on spacecraft surfaces. As the surfaces of a spacecraft may be well below the melting point of a condensable propellant, ions impacting on spacecraft surfaces will stick similarly to the interior of a vacuum tank. This would present a problem for solar arrays and other optical systems, as it is not desirable to have coatings of opaque metals on the transparent lenses and plates of such systems. Other spacecraft integration issues include coating of radiator and dielectric surfaces. Coatings of propellant atoms on radiators will reduce emissivity and radiative efficiency. Dielectrics are very vulnerable to propellant deposition, as conductive coatings on the surface of a dielectric will render it ineffective. Spacecraft design and interaction studies will require future research.

1.6. Feed System for Condensible Propellant Operation

Development of a feed system for a condensible propellant is a major technical obstacle. A large advantage to mercury, as used in NASA thrusters, was that it was a liquid at room temperature; it could be transported through propellant lines with little heat input and the only significant need for external heating was for the evaporator.[40] This system may not be practical for bismuth or the other condensible propellants analyzed here, as the entire propellant feed system would need to be maintained above the melting point of the propellant. This would not present much of a problem for cesium due to the very low melting point, but for bismuth operation, the propellant must be maintained in excess of 271°C. Bismuth thrusters in Soviet research utilized a propellant feed system that was maintained in excess of 1,000°C, in order to flow gaseous bismuth directly into the thruster.[24] Additionally, the thruster body was heated above 1000°C using resistive heaters. This method may present a problem, however, in that a number of heaters consuming significant amounts of power are likely required. While using large amounts of power for a propellant evaporation system is possible in ground testing, any

development of a flight system cannot allow for such expenditures. The use of condensible metal propellants in future Hall thrusters will require development of an energy-efficient feed system. An additional energy expenditure is the evaporation of the propellant, requiring enough heat input to overcome the heat of fusion of the propellant. The energy required to overcome the heat of fusion of the propellant is negligible compared to the total thruster power; Bismuth, for example, requires 54 mW of power per mg/s of mass flow to evaporate.

1.7. Conclusions

For high-I_{sp} missions, krypton may prove advantageous as it provides the highest I_{sp} of the options presented here for a given acceleration voltage, and at such high exhaust energies the large ionization cost is minimized. The erosion rate due to sputtering will also be lower for krypton than other propellants at very high energies (above 10,000 eV). For high-thrust, low-I_{sp} missions, however, the large heavy atoms may provide a benefit. Bismuth provides higher thrust per unit mass than the lighter propellant options given equal accelerating voltages and is very easy to ionize. While cesium is the easiest to ionize, once the average number of collisions in a Hall thruster channel is analyzed, it proves to be only incrementally better than bismuth. Cesium is also only marginally better in the fraction of thruster power required for ionization than bismuth. Heavy atoms also provide an advantage in erosion rate for most ion energies, up to extremely high specific impulses.

Condensible propellants also offer significant advantages over gases. Primary of these is the elimination of the costly and complex pumping apparatus required to maintain acceptable vacuum levels. This benefit is complementary to the increased efficiency of condensable species for low-Isp, and correspondingly high flow rate, missions that are most expensive to ground test. Condensible propellants may cause spacecraft contamination issues, as unlike the gaseous propellants condensibles will deposit on spacecraft surfaces.

Among the condensible propellant options, bismuth shows the most promise for Hall thruster use and is likely superior to other candidates for high-thrust, low-Isp missions. It combines the advantages of higher thrust at the same discharge current as a xenon thruster, low cost, ease of ionization, and lower sputter erosion rate than the other propellants examined. The main disadvantage to bismuth, however, is that any thruster design must incorporate a method of heating the bismuth evaporator to temperatures where evaporation is significant. It is also much less likely that spacecraft surfaces will be warm enough to avoid or reduce bismuth deposition due to the high melting and boiling points. A second, and possibly significant, disadvantage of bismuth may be its propensity to form doubly charged ions at lower electron temperatures than xenon.

References

[1] Praxair, Inc. Verbal quotation, 6/2005, www.praxair.com

[2] Kim, V., Popov, G., et. al., "Investigation of SPT Performance and Particularities of it's Operation with Kr and Kr/Xe Mixtures," 27th International Electric Propulsion Conference, Pasadena, CA, October, 1997. IEPC-01-065

[3] Walker, M.R., "Effects of Facility Backpressure on the Performance and Plume of a Hall Thruster," Ph.D. Dissertation, University of Michigan, 2004.

[4] PHPK Inc. Verbal Quotation for TM-1200 model cryopump, 6/2005

[5] Grishin, S.D., et. al., "Characteristics of a Two-Stage Ion Accelerator with an Anode Layer," Zhurnal Prikladnoi Mekhaniki I Tekhnicheskoi Fiziki 2, p 28-36, March-April 1978

[6] Tverdokhlebov, O.S., and Semenkin, A.V., "Iodine Propellant for Electric Propulsion – To Be Or Not To Be," 37th AIAA/ASME/SAE/ASEE Joint Propulsion Conference, Salt Lake City, UT, July, 2001, AIAA 2001-3350

[7] Bugrova, A.I., Kim, V., et. al., "Physical Processes and Characteristics of Stationary Plasma Thrusters with Closed Electrons Drift," 22nd International Electric Propulsion Conference, Viareggio, Italy, 1991, IEPC-91-079

[8] Dressler, R.A., et. al., "Propellant Alternatives for Ion and Hall Effect Thrusters," 38th AIAA Aerospace Sciences Meeting, AIAA 2000-0602

[9] Kerslake, W.R., and Ignaczak, L.R., "Development and Flight History of SERT II Spacecraft," Journal of Spacecraft and Rockets 30, p.258, 1993

[10] Sovey, J.S., Rawlin, V. K, and Patterson, M.J., "A Synopsis of Ion Propulsion Development Projects in the United States: SERT I to Deep Space I," AIAA 99-2270, NASA TM-1999-209439

[11] See, for example, http://www.osha.gov/SLTC/cadmium/, accessed 6/2005

[12] See, for example, http://www.espi-metals.com/msds's/cesium.htm, accessed 6/2005

[13] See, for example, http://www.jtbaker.com/msds/englishhtml/i2680.htm, accessed 6/2005

[14] See, for example, http://www.jtbaker.com/msds/englishhtml/M1599.htm, accessed 6/2005

[15] See, for example, http://minerals.usgs.gov/minerals/pubs/commodity/bismuth/bismumyb03.pdf

[16] See, for example, minerals.usgs.gov/minerals/ pubs/commodity/cadmium/cadmmyb02.pdf

[17] Catalog price $198/5g 99.999% purity, from Sigma-Aldrich, Inc., www.sigmaaldrich.com

[18] Catalog price $242/500g USP, from Sigma-Aldrich, Inc., www.sigmaaldrich.com

[19] Praxair, Inc. Verbal quotation, 6/2005, www.praxair.com

[20] See, for example, http://minerals.usgs.gov/minerals/pubs/commodity/mercury/430798.pdf, accessed 6/2005

[21] See, for example, http://www.vngas.com/pdf/g54.pdf, accessed 6/2005

[22] See, for example, http://www.scottecatalog.com/msds.nsf/0/86e8c8fec163c40985256a0a004e2f4c?OpenDocument, accessed 6/2005

[23] See, for example, http://www.sciencestuff.com/msds/C1309.html, accessed 6/2005

[24] Tverdokhlebov, S., Semenkin, A., and Polk, J., "Bismuth Propellant Option for Very High Power TAL Thruster," 40th AIAA Aerospace Sciences Meeting, AIAA 2002-0348

[25] Massey, D.R, King, L.B., and Makela, J.M., "Progress on the Development of a Direct Evaporation Bismuth Hall Thruster," 41st Joint Propulsion Conference, 10-13 July 2005, Tucson, AZ, AIAA 2005-4232

[26] Freund, R.S., et. al., "Cross-Section Measurements for Electron-Impact Ionization of Atoms," Phys. Rev. A 41(7), p. 3575, 1 April 1990 (APS)

[27] Nygaard, K.J., "Electron-Impact Ionization Cross Section in Cesium," J. Chem. Phys. 49(5), p.1995, 1 September 1968 (AIP)

[28] McFarland, R.H., and Kinney, J.D., "Absolute Cross Sections of Lithium and Other Alkali Metal Atoms for Ionization by Electrons," Phys. Rev. 137(4A), p.A1058, 15 February 1965 (APS)

[29] Hayes, T.R., et. al., "Absolute Electron-Impact-Ionization Cross-Section Measurements of the Halogen Atoms," Phys. Rev. A. 35(2) p. 578, 15 January 1987 (APS)

[30] Wetzel, R.C., et. al., "Absolute Cross Sections for Electron-Impact Ionization of the Rare Gas Atoms by the Fast-Neutral-Beam Method," Phys. Rev. A. 35(2) p.559, 15 January 1987 (APS)

[31] Kieffer, L.J., and Dunn, G.H., "Electron Impact Ionization Cross-Section Data for Atoms, Atomic Ions, and Diatomic Molecules: I. Experimental Data," Rev. Mod. Phys. 38(1) p.1, January 1966 (APS)

[32] Gombosi, T.I., Gaskinetic Theory, Cambridge University Press, 1994, ISBN 0-521-43966-3

[33] Haas, J.M., and Gallimore, A.D., "Considerations on the Role of the Hall Current in a Laboratory-Model Thruster," 37th AIAA/ASME/SAE/ASEE Joint Propulsion Conference, Salt Lake City, UT, July 2001, AIAA 2001-3507

[34] Meezan, N. B., Hargus, W.A., and Cappelli, M.A., "Anomalous Electron Mobility in a Coaxial Hall Discharge Plasma," Phys. Rev. E. 63, 026410

[35] Bishaev, A.M., and KIM, V., "Local Plasma Properties in a Hall-Current Accelerator with an Extended Acceleration Zone," Sov. Phys. Tech. Phys. 23(9), p.1055

[36] King, L.B., Transport-property and Mass Spectral Measurements in the Plasma Exhaust Plume of a Hall-effect Space Propulsion System, Ph.D. Dissertation, University of Michigan, 1998.

[37] Nastasi, Michael, Mayer, James W., and Hirvonen, James K., Ion-Solid Interactions Fundamentals and Applications, Cambridge University Press, 1996, ISBN 0-521-37376-X

[38] Raitses, Y. and Fisch, N.J., "Parametric Investigations of a Nonconventional Hall Thruster," Phys. Plasmas 8(5), p. 2579, May 2001 (AIP)

[39] Raitses, Y., Keidar, M., et. al., "Effects of Segmented Electrode in Hall Current Plasma Thrusters," J. Appl. Phys. 92(9), p.4906, 1 November 2002 (AIP)

[40] Kerslake, William R., "Design and Test of Porous-Tungsten mercury Vaporizers," 9th AIAA Electric Propulsion Conference (AIAA 72-484), Bethesda, MD April 17-19, 1972

2. Description of Concept and Apparatus

2.1. Direct Evaporation

While physically superior in the discharge chamber, the obvious engineering challenge associated with bismuth is how to produce and deliver a metered flow of vapor to the thruster in an energy efficient method. A straightforward approach to a Bi mass-flow system might be to heat a reservoir of the metal to high temperatures to induce evaporation and transfer the vapors through heated plumbing to the anode/gas diffuser. This approach was used in early Soviet work.[1,2] Besides the material difficulties associated with high-temperature propellant isolators, valves, and flow control devices, such a system is energetically unfavorable. Any power that is used to drive the evaporation heater and to maintain the temperature of the transfer plumbing is non-propulsive and reduces the overall system efficiency of the thruster. A system-level analysis of the resistively heated supply scheme is shown in Figure 2-1.

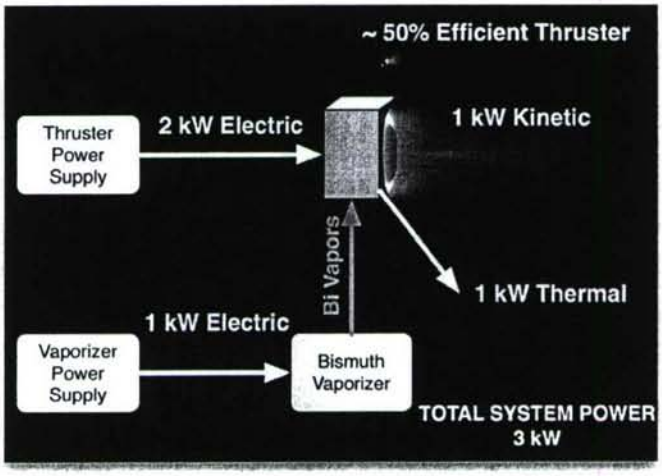


Figure 2-1. System power for an externally heated bismuth supply system.

In the method proposed here, bismuth is supplied to an anode/reservoir within the thruster discharge chamber in solid or liquid form. Naturally occurring thruster waste heat is used to drive direct evaporation from the anode/reservoir into the discharge chamber. The evaporation rate is controlled through the reservoir temperature. The concept developed and patented by MTU (US Patent No. 7,059,111) is shown in Figure 2-2.

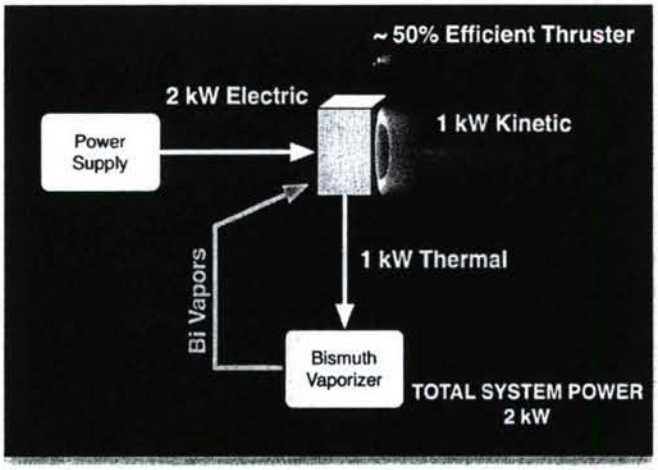


Figure 2-2. MTU-patented energy harvesting scheme to use plasma discharge waste heat from electron attachment to the anode for bismuth evaporation.

Since it is not feasible to mechanically vary the vapor escape area through the reservoir, the mass flow rate, $\dot{m}$ will be controlled by varying the reservoir temperature within the thruster. The evaporation rate, then, is governed by the equilibrium vapor pressure of the liquid metal and the goal is to maintain the proper reservoir temperature that, when combined with the vapor escape area, yields the correct value of mass flow.

2.2. The Segmented Anode Hall Thruster

Control of anode/reservoir temperature is necessary to control the flow of bismuth. In order to control the temperature of the main anode, a pair of inert shim electrodes was added to the discharge channel of the thruster, downstream of the main anode, as shown in Figure 2-3. By slightly varying the shim electrode voltage with respect to the main anode/reservoir, the discharge current can be shifted between the shim electrodes and the main anode. This shift in discharge current will then shift the discharge heating, with the result that shifting current to the shims will cool the main anode, and diverting current back to the anode will increase its temperature, and hence the bismuth evaporation rate.[1] The shim electrodes were fabricated from nonmagnetic stainless steel so as to impact the magnetic field of the thruster as little as possible. A schematic of the electrical diagram is shown in Figure 2-4.

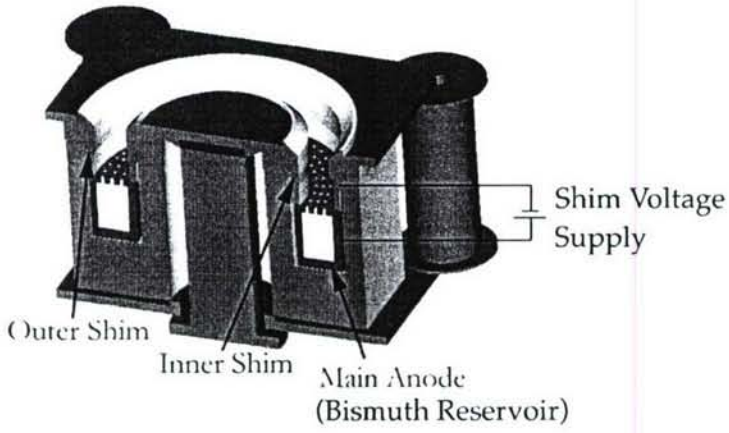


Figure 2-3. Cross section of segmented-anode thruster for direct evaporation of bismuth. The shim electrodes can be used to intercept a fraction of the discharge current and, hence, control the heat deposition to the main anode/bismuth reservoir.

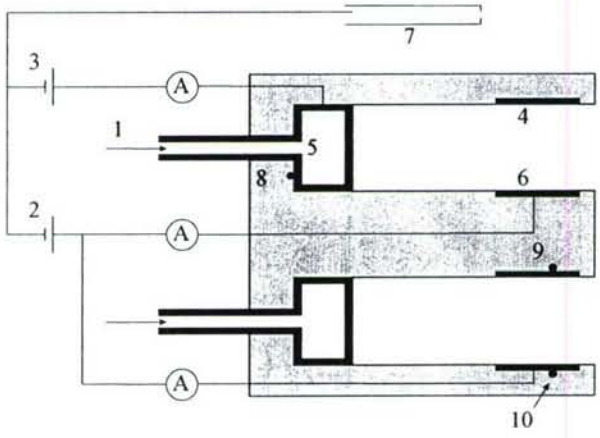


Figure 2-4. Electrical schematic of thruster test apparatus. Numbered annotations are 1: xenon propellant flow (for test with Xe instead of Bi), 2: shim power supply, 3: main anode power supply, 4: outer shim electrode, 5: main anode and gas distributor, 6: inner shim electrode, 7: cathode, 8: anode thermocouple, 9: inner shim thermocouple, and 10: outer shim thermocouple.

The goal of the segmented anode design was to maintain the proper reservoir temperature that, when combined with the vapor escape area from the porous anode face, yields the correct value of mass flow.

$$P_v = \log^{-1}\left[13.317 - \frac{10{,}114}{T} - 0.86\log T\right] \qquad 2\text{-}1$$

$$\dot{m} = \frac{P_v}{\sqrt{\frac{2\pi kT}{m}}} A \qquad 2\text{-}2$$

Equation 2-1 gives the vapor pressure, P_v in Pascals for bismuth where T is the temperature in Kelvin[2] and Eqn. 2-2 gives a kinetic expression for the evaporation rate through some free-surface area, A. Using equations 2-1 and 2-2 it is then possible to calculate the evaporation rate per-vapor-escape-area $\dot{m}$ /A as a function of reservoir temperature.

Figure 2-5 illustrates the mass flow rate per-unit-area as a function of reservoir temperature for an evaporative bismuth source. This plot can be used to estimate the required reservoir temperature for a candidate Hall thruster if the anode were used as the reservoir. For instance, a typical 2-kW-class Hall thruster has about 3,700 mm^2 of exposed anode face and runs on 5.4 mg/sec of propellant. Figuring on a 10% open area on the anode face, a temperature of about 750°C will provide the necessary mass flow rate.

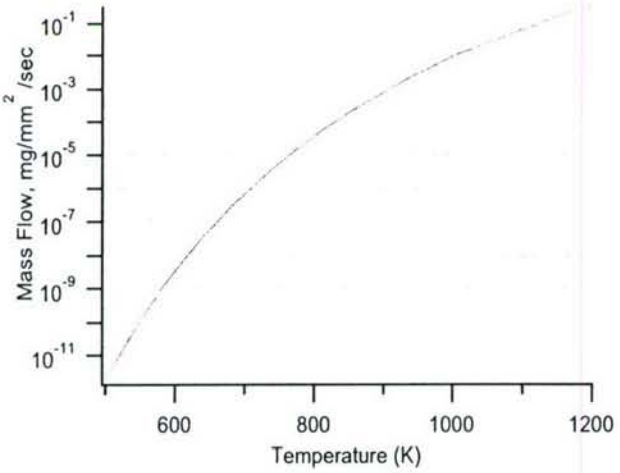


Figure 2-5. Calculated Bi evaporation rate as a function of temperature.

The design goal is then to 1) achieve an anode/reservoir temperature on the order of 750 deg C using only the waste heat from the discharge, and 2) implement some type of temperature control scheme to enable closed-loop control of the evaporation rate through the fixed vapor escape area. Thermal modeling was conducted to evaluate the temperature range and, hence mass-flow range, that can be expected within the proposed device. Figure 2-6 is a composite image of two different test cases analyzed for the thruster used in subsequent laboratory testing. In the top case, all of the discharge current was placed into the main anode which, for the 2-kW device considered here, was estimated to produce a 10%, or 200 W, heat input. In the bottom case, all of the power was placed into the inner shim anode. As can be seen, temperature changes on the main anode varied by approximately 50°C. Because of the steep slope of the bismuth vapor pressure curve, a ΔT of 50°C would enable nearly an order of magnitude throttleability in mass flow.

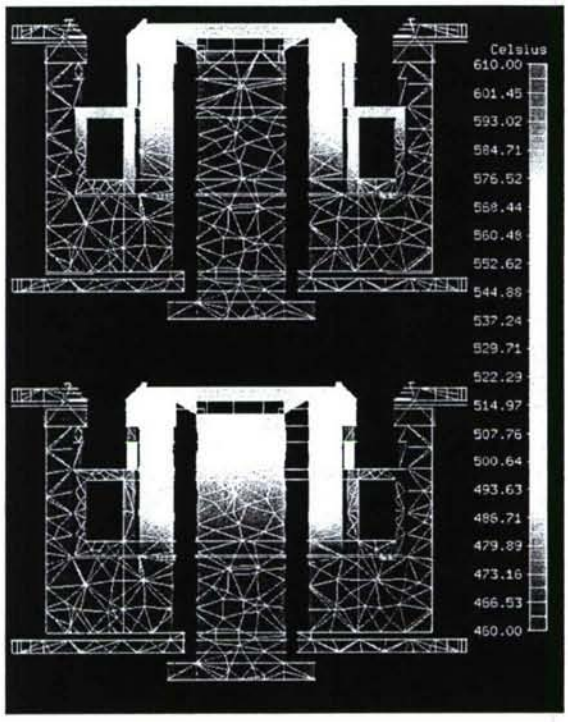


Figure 2-6. Thermal simulation of segmented anode thruster. In the top figure, 100% of the discharge current is attached to the main anode. In the bottom, all of the current is intercepted by the inner shim electrode.

The thruster used was a modified Aerojet BPT-2000 Hall thruster. While the overall geometry and magnetic circuitry of the BPT-2000 was preserved, the interior electrode structure was modified to accommodate the three-electrode configuration pictured in Figure 2-3. In order collect thermal data, thermocouples were placed at seven different locations on the thruster – back of the main anode, outer shim, inner shim, magnets, cathode mount, main propellant line and thruster mounting plate. A photograph of the thruster is shown in Figure 2-7.

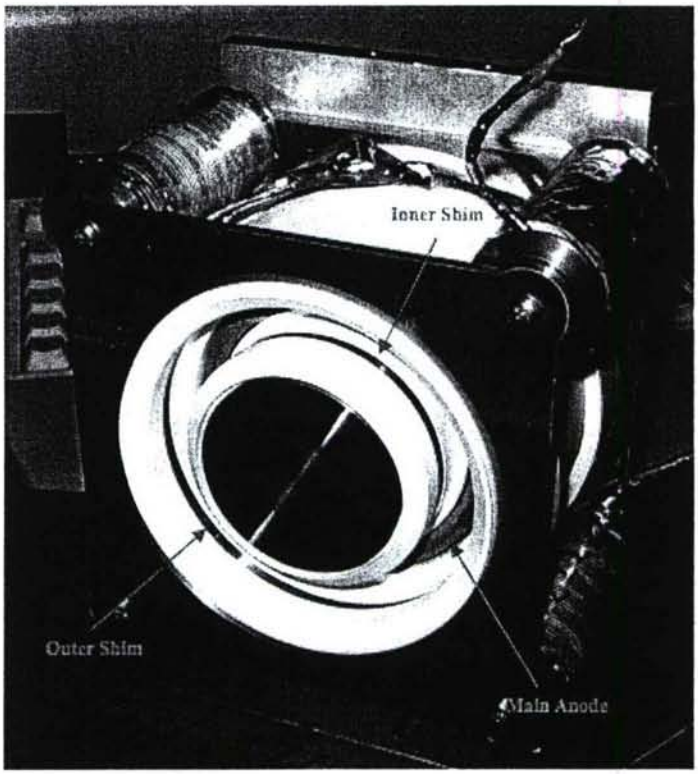


Figure 2-7. Photograph of segmented-anode Hall thruster based on the Aerojet BPT-2000.

---

[1] Massey, D.R., King, L.B., et. al., ":Progress on the Development of a Direct Evaporation Bismuth Hall Thruster," 41st Joint Propulsion Conference and Exhibit, Tucson, AZ, 10-13 July 2005, AIAA-4232

[2] Gray, D.E., ed., American Institute of Physics Handbook 3rd Edition, McGraw-Hill, 1972.

3. Segmented-Anode Thruster Performance: Xenon

3.1. Motivation for Xe Testing

While the segmented electrodes present a unique thermal control strategy, the non-traditional configuration may cause a change in the operating characteristics of the thruster. Any negative impact on beam divergence, efficiency, Isp, or thrust could negate the anticipated performance benefits of the bismuth scheme. One use of segmented electrodes in previous studies was as a method of achieving two-stage operation,[1] where the shim electrodes are maintained at a potential between the anode and the cathode, allowing for an acceleration-only stage for high specific impulse operation. Other experimental investigations have been performed on segmented-electrode Hall thrusters and showed a net decrease in beam divergence and an increase in thrust with addition of the segmented electrodes.[2,3,4] These investigations were performed on thrusters with very different operating parameters than the design implemented in this paper. In many of the experiments, the shim electrodes were held either at anode potential, cathode potential, or just allowed to float (as opposed to being forced to accept varying fractions of the discharge current). Some of the shim electrode configurations previously investigated were also emissive in nature. Between the differences in materials, thruster operating regime, and the method of power application to the shim electrodes any attempt to predict the behavior of a candidate segmented anode bismuth thruster, particularly at moderate power levels, is necessarily precluded without experimental observation. Previous experiments on a similar thruster design intended for bismuth operation showed little change in the beam profile[5] or performance.[6]

The first goal of Xe testing was to determine the effect, if any, the addition of shim electrodes have on the performance of a 2-kW Hall thruster. The second goal was to determine the source of these changes, if any. Plasma probes were utilized to determine the beam divergence, ion energy, and multiply charged ion fraction in the thruster plume, to determine the source of any performance change.

3.2. Xe Test Facility and Apparatus

3.2.1. Vacuum Facility and Test Bed

All tests were performed in the I_{sp} Lab's Xenon Test Facility (XTF). The facility is comprised of a 2-m-diameter by 4-m-long vacuum tank. Rough pumping is accomplished by a two-stage rotary oil-sealed vacuum pump with a Roots blower, capable of pumping at 200 l/s. High vacuum is achieved through dual 48-inch-diameter cryopumps, capable of a combined pumping rate of 120,000 l/s on nitrogen as in Figure 3-1. Tank pressure was measured via a Bayard-Alpert ionization gauge mounted behind the thruster, on one of the end-caps of the tank. The probes utilized in the characterization of the thruster plume were mounted on a motion table with two linear axes, one parallel to the tank axis and one horizontal and perpendicular to tank axis. Rotation about the vertical axis was accomplished through use of a rotary stage. The motion tables were controlled via servomotor. A photograph of the thruster installed on the thrust stand is shown in Figure 3-2.

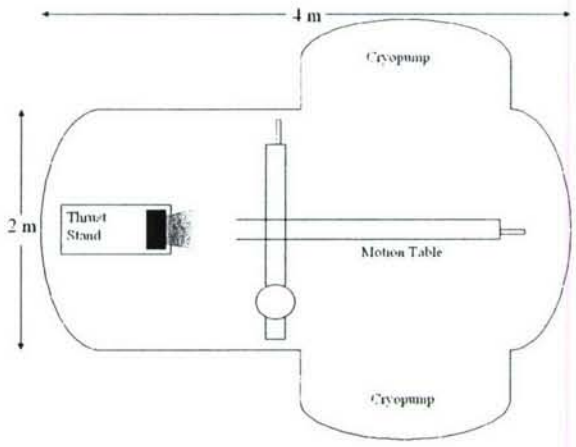


Figure 3-1. Top view of Xe test facility.

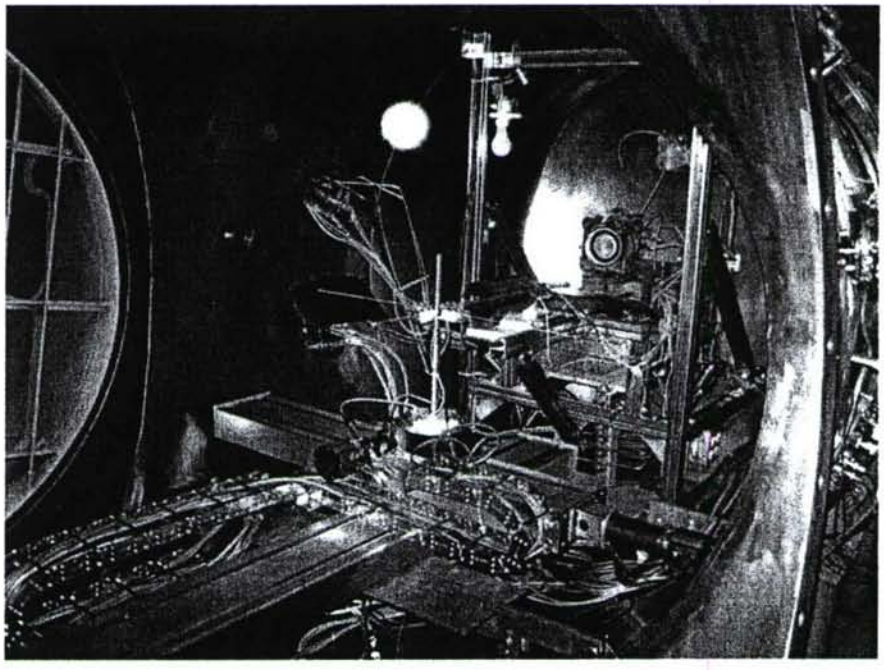


Figure 3-2. Thruster mounted on thrust stand in Xe test facility at the Isp Lab.

3.2.2. Performance Measurements

Thrust measurements were taken using an inverted pendulum thrust stand[7] and recorded via a computer-controlled data acquisition system. Thrust stand tilt was monitored by use of a tilt sensor and adjusted through a stepper motor and jack screw. Voltage and current measurements were measured directly by the power supplies and recorded on the computer simultaneously to the thrust measurements.

3.2.3. Faraday Probe

A Faraday probe is a planar electrostatic probe,[8,9,10] biased negative relative to the plasma floating potential in the ion saturation regime. Biasing to this voltage allows the probe to pull in the ions in the discharge, while rejecting discharge electrons. Data are acquired by sweeping the probe across the face of the thruster, and measuring the current collected at each point in the sweep. Faraday probe sweeps are usually circular arcs at a constant radius from the thruster, allowing the current measurements to represent the relative flux of ions as a function of distance or angle from the thruster axis. Distance from the thruster has a large effect on ion density. Eliminating this as a factor in the ion current measurement allows determination of the plume divergence.

The Faraday probe utilized in the work reported here consisted of a 2.4-mm-dia. tungsten electrode enclosed in an alumina tube with diameter 4 mm. The guard ring was constructed of stainless steel and surrounded the alumina tube at the end of the probe. Measurements were taken using a Keithley 2410 sourcemeter. Performing an I-V sweep and finding the voltage where the probe was fully in the ion saturation regime determined the bias voltage. The guard ring was operated on a separate power supply, set to the same voltage as the sourcemeter. Faraday probe scans were performed at 250 mm from the thruster exit, sweeping through off-axis distances of 200 mm on either side of the thruster axis. These off-axis distances corresponded to an off-axis angle of 53.1 degrees. The sweeps were divided into 51 equally spaced points 2.124 degrees apart, such that the distance between points in the sweep was 9.3 mm. Two measurements were made at every point in the probe sweep, allowing for determination of the sample variance of the current measurement.

3.2.4. Retarding Potential Analyzer

A Retarding Potential Analyzer (RPA) is a gridded probe which is used to determine the directed ion energies present in a plasma[11] and has been used to good effect in Hall thruster plume studies.[12,13] An RPA provides a decelerating voltage, which ions must be able to pass in order to be detected. If this voltage is much smaller than the accelerating potential hill in the thruster, all of the beam ions will pass and be collected. If the retarding potential is larger than the accelerating potential in the thruster, no ions will be collected. In this way, an RPA functions as a high-pass filter, allowing only those ions of sufficient energy to pass the retarding potential to be detected.

The RPA utilized in the experiments reported here is of the four-grid design. All conductive components of the RPA are constructed from stainless steel. The grids are fabricated from stainless steel mesh with a 0.139-mm average grid gap, and 30% open-area fraction. The electrical connection to the grids are made via stainless-steel wire, run through the casing of the probe and welded to each grid. Alumina-silicate ceramic spacers separate the grids. The entry orifice of the probe is 12.7 mm in diameter. The front face of the probe is fastened with screws to the outer casing, and serves to press the grids and spacers together, preventing any movement during testing. The entry grid of the probe was in contact with the front face, and thus was floating at all times during testing.

The ion repeller grid of the RPA was swept from zero to as much as 600 V above ground. The maximum voltage varied according to thruster operating point; higher thruster voltages required higher ion repeller voltages to filter out all of the beam ions. Sweeping was accomplished through use of a Keithley 2410 in voltage sweep mode. Electron and secondary electron repeller grids were set at 10 V below ground and remained at the same potential through the entire testing sequence. The value of 10 V was chosen so as to be significantly higher than

the voltage necessary to reject the plasma electrons on the electron repeller grid, which usually required a potential of only 2 V below ground. The current to the collector was amplified and converted to a voltage signal by an analog current amplifier, with a gain setting of either 10^3 or 10^4 volts per amp, dependent on the thruster operating point. An oscilloscope then read this voltage. The ion repeller voltage controlled the oscilloscope triggering, so that the current detected by the probe as a function of voltage could be easily extracted. The RPA measurements were referenced to plasma potential, which was measured by an emissive probe.

3.2.5. Emissive Probe

An emissive probe consists of a hot filament, heated such that it will emit electrons.[14] At potentials below the plasma potential, the plasma electrons will be deflected away from the probe due to its negative potential relative to the plasma repelling the electrons. At potentials above the plasma potential, the probe will attract and collect plasma electrons. The purpose of the emission is that when the probe is below plasma potential, it will emit electrons, which are immediately repelled from the probe by the difference between it and plasma potential. For potentials above plasma potential, any emitted electrons are attracted to the filament by its high potential relative to the plasma, and thus provide no net current. This change in behavior between potentials above and below plasma potential causes a large change in incident current on the probe due to the plasma.

The plasma potential can then be found by examining the intersection between the shallow electron saturation regime and the steep emissive regime. The specific method used for this was to find a linear fit to the I-V characteristic in both the emission and electron saturation regimes, and find the point where the two fits intersected.[15] The voltage at the intersection was the plasma potential.

The emissive probes utilized consisted of 0.127-mm-diameter thoriated tungsten filaments (2% thorium content). The purpose of the thorium is to reduce the work function of the material, increasing the emission current and allowing the probe to be operated at lower temperatures. The probe filaments were approximately 5 mm long. Current was passed along the filaments to heat them to incandescence and allow them to emit electrons. The current necessary for onset of electron emission was approximately 2.6 amps, and the hot probes exhibited a resistance of approximately 2 ohms, varying slightly from probe to probe.

3.2.6. ExB Probe

An ExB probe uses perpendicular electric and magnetic fields to filter ions by velocity. ExB probes have been successfully used for characterization of Hall thruster plasmas by several researchers.[16] This is an important distinction from the filtering in an RPA. Due to the electrostatic nature of the RPA, it cannot distinguish between singly- and multiply-charged ions of the same energy per unit charge. The filtering in an ExB probe is based purely on ion velocity. As it is independent of charge state, the multiply-charged ions, which are typically traveling faster than singly-charged ions, can be resolved and their fraction of total density calculated. The magnetic field in an ExB probe is typically supplied by permanent magnets, as the magnetic field supplied by permanent magnets does not vary with time and is not dependent on current or core material as in electromagnets. Two parallel plates, placed on either side of the ion path, supply the electric field. These act like a parallel-plate capacitor, providing an electric field dependent only on the distance between the plates and the applied voltage.

Development of density fractions of ions from an ExB probe is nontrivial. The probe provides the total distribution of ions of each species, and each peak of the trace takes into account the energy resolution error of the probe. This makes use of the Maxwell or Druyvestyn ion energy distributions problematic. A method first used by Kim[17] and later used by Hofer[18] was to assume that prior to acceleration all ions had the same temperature. Thus when the ions were accelerated, the original ion temperature would determine the β in the Maxwellian or Druyvesteyn models, and each population of ions in the distribution would have the same characteristic width. Due to the nature of the Maxwellian and Druyvestyn fits, however, the area under a distribution (and hence, the relative population of ions which that distribution describes) is directly proportional to the maximum height of the distribution and the width of the distribution. Width is described by β, and thus is the same for all populations of ions in the distribution. Thus the height is the only important factor in calculating the multiply charged ion fraction, and the need to perform a curve fit of multiple distribution functions (one for each peak in the distribution) is unnecessary. This method produced good results on an SPT-100 thruster as measured by Kim, with the multiply charged ion fractions showing good agreement with measurements taken using other methods by King[19] and Manzella.[20]

The ExB probe utilized in the experiments reported here had a 5-cm collimator and a 23-cm filter. The orifices in the collimator plates were 1.6 mm in diameter. The orifice in the filter exit plate was 2.4 mm in diameter. All of the orifices had 90-degree chamfers on their downstream sides, to prevent ions from hitting the interiors of the orifices and unnecessarily reducing the measured current. The magnetic field was supplied by two 5-cm x 23-cm x 1.3-cm banks of NdFeB rare earth magnets. Rare earth magnets, with their very high field strength, were chosen to improve the resolution of the probe over that available with ceramic magnets. The magnets were separated by Teflon spacers, which also held and insulated the electrode plates from the structure of the probe. The current was read by a K and M Electronics model 7550m channel electron multiplier. The multiplier was operated at a supply voltage of –2330 V, which correlated to a gain of up to 10^8 A per amp of ion current collected. The casing of the probe as well as the three orifice plates were fabricated of magnetic stainless steel, to direct and focus the magnetic field while preventing oxidation as is typical of magnetic iron or mild steels. The output current of the electron multiplier was converted to a voltage signal via the current amplifier used with the RPA. The gains were much higher than in the RPA experiments, however, ranging from 10^6 to 10^8 V per amp, for a total system gain of 10^{14} to 10^{16} volts per amp. Tuning of the electrodes and thus the electric field in the probe was performed by use of a Keithley 2410 sourcemeter, which typically swept the voltage from zero to 300 V at a rate of 0.5 Hz. The output of the sweep power supply was passed through a voltage divider with a grounded center tap, allowing one of the plates to be biased at half the total electrode voltage positive, and the other plate an equal distance below ground. The splitting of the sweep voltage was to prevent any deceleration effects in the probe. If one electrode was at a high potential while the other was grounded, the potential at the centerline of the probe (halfway between the electrode plates) is approximately half the applied voltage. This behaves as a potential hill similar to that in an RPA. In an ExB probe, however, deceleration of the ions will prevent proper filtering of velocity, as the ions are unnecessarily slowed as they enter the probe. Forcing the electrodes to equal voltages above and below ground allows the potential at the centerline of the probe to be at or near ground, thus eliminating any deceleration of the ions. The probe included a water cooled shell which prevented excessive heating of the probe components. This was especially important as the NdFeB magnets have a low thermal tolerance.

Calibration of the ExB probe was accomplished by comparing the most probable ion energies calculated by the RPA analysis and the most probable ion energies obtained from the probe. As the probe voltage is directly related to velocity and energy is proportional to the square of velocity, the square of the probe voltage is proportional to energy and the calibration must be

performed with the square of the probe voltage as the independent variable. The ExB probe was calibrated using the raw RPA data, before compensation for plasma potential.

3.3. Results

3.3.1. Thermal Performance

The variation in anode/shim electrode temperature as a function of current attachment was investigated. To establish the range over which the temperatures could be controlled, the thruster was allowed to come to thermal equilibrium with the current completely attached to each electrode. Figure 3-3 shows how the thruster responds to both current shifting and mass flow increases with the main anode voltage fixed at 400 volts. The main anode temperature varied between approximately 425 °C at 5 mg/s with all current on the shim electrodes to nearly 600 °C at 7 mg/sec with current on the main anode.

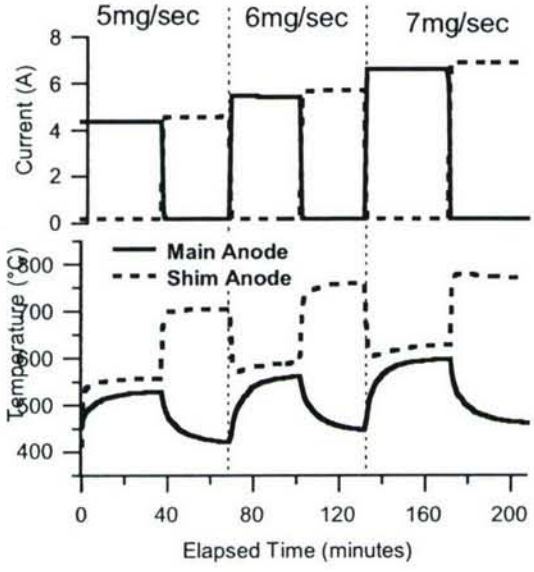


Figure 3-3. Thermal response of the segmented-anode Hall thruster with 400 V on the main anode. Temperature uncertainty is approximately 1%.

3.3.2. Thrust Performance

Propellant mass flow rate, anode voltage, and the level of discharge current on the shims were each used as experimental factors. Three levels of mass flow and anode voltage were used, as well as five levels of discharge current on the shims. Xenon was provided to the thruster at a rate of 4, 5, and 6 mg/s. The anode voltage was 300, 350, and 400 V. The level of discharge current on the shims was set to 100%, 75%, 50%, 25%, and <5% of the total current. A small amount of current had to be maintained at all times on the shims to maintain thruster stability.

Shim current was regulated by adjustment of the shim voltage. Setting the shim voltage higher than the anode forced all current to the shims, while setting it lower than the anode sent current back to the anode. A sample plot of the current on the shims and the main anode, as well as the total discharge current, is included in Figure 3-4. The other combinations of mass flow and anode voltage have similar current characteristics. Additionally, the complete test matrix performed, with voltages and currents for every operating point examined are in Table 3-1.

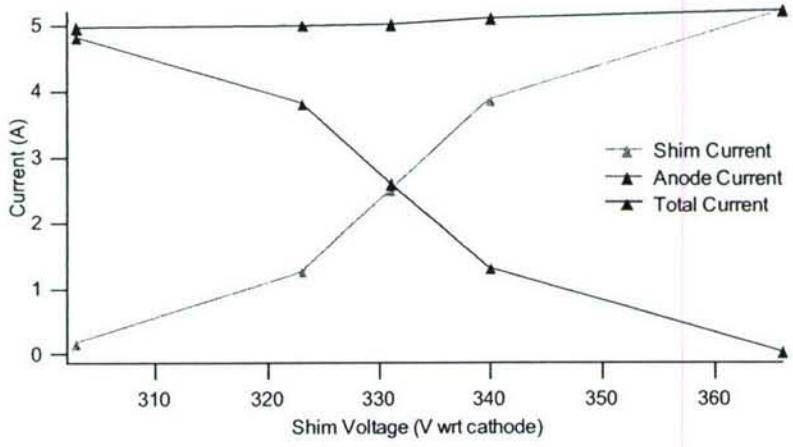


Figure 3-4: Characteristic shift in current on the shims and main anode as shim voltage was varied. Thruster was operating at 350 V on the anode and 5 mg/s of mass flow.

There are two roughly linear regions in the current characteristic. The extremes of the characteristic show a roughly equal shallow slope, while the center of the characteristic has a much higher slope. This indicates that the change in voltage necessary to adjust the current attachment when it is equally shared between the main anode and the shims is much smaller than that required to force all of the current to either the shims or the main anode. This can complicate fine control of the level of discharge heating on either the shims or the main anode, as points in the center of the characteristic are very sensitive to small changes in voltage. An unexpected result of shifting all of the discharge current to the shims is that the voltage required to do so is higher than the anode voltage.

. Plotting the thrust measured for each anode voltage and mass flow combination as a function of shim voltage showed the general trends in thrust as all three factors were varied, as shown in Figure 3-5. The first two conclusions to be drawn from these data are that thrust increased with mass flow and with anode voltage. Both these conclusions are expected; an increase in anode voltage (and the corresponding increase in shim voltage required to divert electron heating to the desired location) will accelerate the ions to higher velocities than a low voltage, and hence, increase the thrust force. Increased mass flow will also directly increase the thrust force, assuming the ion acceleration mechanism (and hence, ion velocity) is unaffected. Additionally, the thrust appears to increase with shim voltage, a trend which indicates ion acceleration is dictated at least somewhat by the shim voltage.

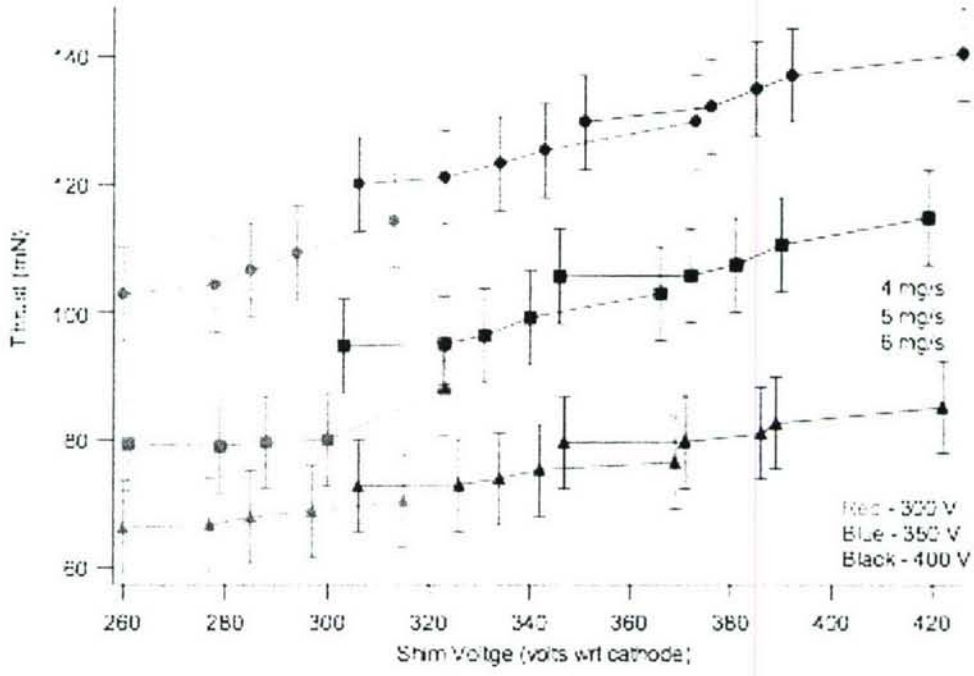


Figure 3-5: Thrust measured as a function of all three experimental factors. Higher shim voltages for a given mass flow and anode voltage combination correspond to higher discharge heating acceptance by the shims.

Application of the analysis of variance method of error analysis can determine both the confidence that an experimental factor has a significant effect on a measurement, as well as generate a confidence interval of the data. [21] The P-values calculated by this method represent the probability that a factor does not have an effect on a measurement. The calculated P-values ranged between 2.3×10^{-30} and 6×10^{-5}; much less than 1%, leading to the conclusion that each experimental factor had a significant effect on the thrust. The width of the 95% confidence interval on the thrust data, is calculated to be 6.68mN by use of the t-distribution and the estimate of the variance on the data from the analysis of variance method. This is a moderate uncertainty, ranging from 5-10% of the measured values of thrust. This uncertainty could be greatly reduced if further testing of the thruster was performed, allowing a reduction in the t-distribution value used as well as a reduced contribution from the sample variance.

Specific impulse of the thruster at all operating points is plotted in Figure 3-6. The trends in specific impulse are similar to thrust; specific impulse appeared to increase with all three factors. A notable exception to this is the specific impulse at 300 V on the main anode and 5 mg/s of mass flow. In this case the specific impulse was lower than that seen at 300 V and 4 mg/s, the opposite of the trend seen at the other operating points.

Analysis of variance shows that, similarly to thrust, the specific impulse sees a significant effect from all three factors. The P-values for each factor are extremely small, ranging from 5.3×10^{-25} to 3.7×10^{-8}. Similarly to thrust, this indicates that the specific impulse saw a statistically significant change as each experimental factor was modified. The width of the 95% confidence interval was 92.3 s, or roughly 4% of the measurement.

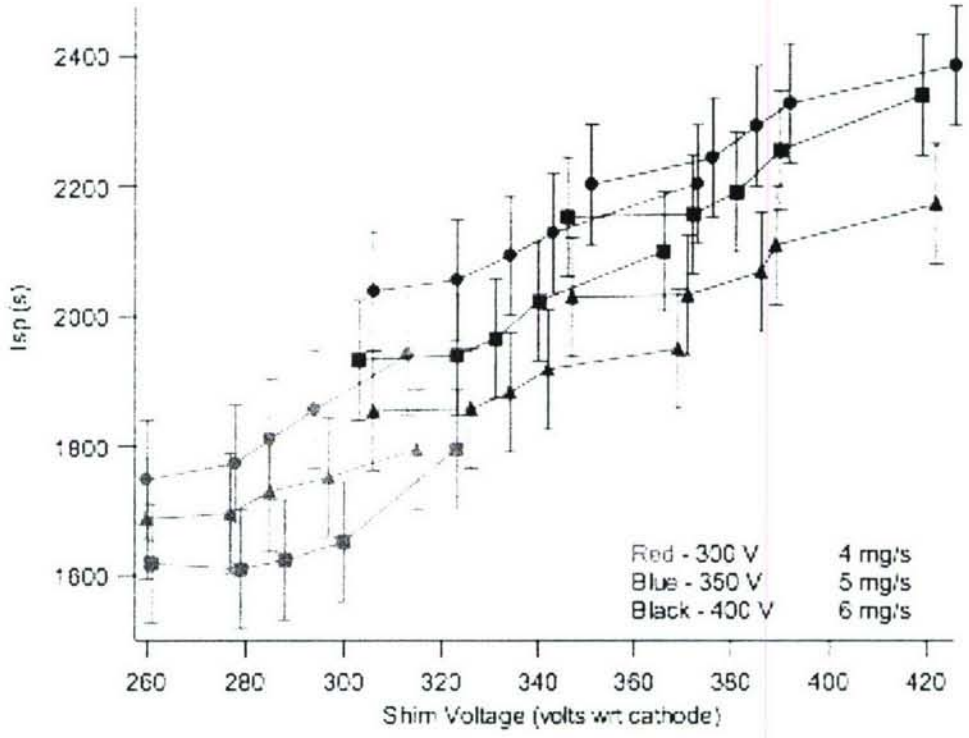


Figure 3-6: Specific Impulse as a function of shim voltage for all thruster operating conditions tested. Higher shim voltage for a given anode voltage indicates higher discharge electron heating on the shims.

Thruster anode efficiency was calculated from the power and propellant mass flow supplied to the thruster and the thrust output. Efficiency for all thruster operating points is plotted in Figure 3-7. Similarly to thrust and specific impulse, the data indicate a significant dependence on anode voltage and mass flow. The increase in thruster efficiency with thruster voltage was expected, and has been seen in previous thruster investigations.[22,23] Unlike thrust and specific impulse, however, the efficiency change with shim voltage does not appear to indicate that there is a significant effect on the efficiency as a function of shim voltage.

Examining the efficiency data through use of the analysis of variance shows that the conclusions reached by initial visual inspection are correct. The P-values for anode voltage and mass flow were 9.5×10^{-12} and 3.5×10^{-7}, respectively; indicating both had a significant effect on the anode efficiency. The P-value of 0.522 for the discharge electron heating level, which corresponds to a 52.2% certainty that the shim current has no effect on efficiency, is large enough that it can be said with good confidence that the location of discharge electron heating does not significantly affect the efficiency of the thruster. The 95% confidence interval on efficiency has a width of .0526. This uncertainty is large relative to the measurements themselves; at best, the uncertainty is 8.6% of the measurement, and at worst it is 13% of the measurement; a much larger uncertainty than that seen in the specific impulse or thrust data.

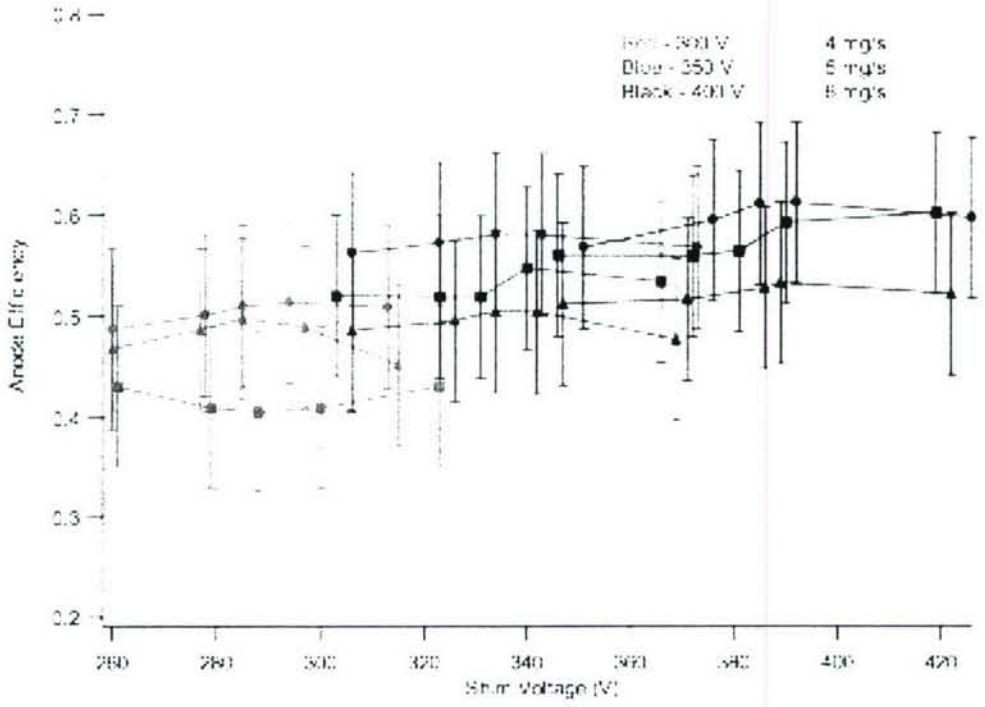


Figure 3-7:Thruster Efficiency as a function of all three experimental factors. Higher shim voltage for a given anode voltage indicates higher discharge heating on the shims.

Table 3-1. Thruster operating conditions examined.

Anode Voltage	Anode Current	Shim Voltage	Shim Current	Total Current	Total Power	Operating Point Label
4 mg/s of xenon						
300 V	0	323	4.14	4.14	1304.1	304100
	1	300	3.11	4.11	1223.7	30475
	2.1	288	2.09	4.19	1225.7	30450
	3.08	279	1.03	4.11	1209.3	30425
	3.88	261	.15	4.03	1203	3040
350 V	0	366	4.07	4.07	1501.8	354100
	1.01	340	3.02	4.03	1386.3	35475
	2.01	331	2	4.01	1371.5	35450
	2.98	323	.99	3.97	1365.7	35425
	3.75	303	.15	3.9	1356.4	3540
400 V	0	419	4.08	4.08	1321.8	404100
	1.01	390	3	4.01	1571	40475
	1.98	381	1.98	3.96	1556.3	40450
	2.98	372	.94	3.92	1481.6	40425
	3.75	346	.15	3.9	1552.1	4040
5 mg/s of xenon						
300 V	0	323	5.18	5.18	1673.1	305100
	1.3	300	3.92	5.22	1566	30575
	2.59	288	2.6	5.19	1525.8	30550
	3.77	279	1.27	5.04	1485.3	30525
	4.73	261	.15	4.88	1458.2	3050
350 V	0	366	5.21	5.21	1906.9	355100
	1.25	340	3.84	5.08	1743.1	35575
	2.5	331	2.5	5	1702.5	35550
	3.74	323	1.24	4.98	1709.5	35525
	4.8	303	.15	4.95	1725.5	3550
400 V	0	419	5.2	5.2	2178.8	405100
	1.28	390	3.83	5.11	2005.7	40575
	2.52	381	3.53	5.04	1968.1	40550
	3.74	372	1.27	5.01	1968.4	40525
	4.85	346	.15	5	1991.9	4050
6 mg/s of xenon						
300 V	.01	313	6.38	6.39	1999.9	306100
	1.55	294	4.7	6.25	1846.8	30675
	3.14	285	3.14	6.28	1836.9	30650
	4.68	278	1.57	6.25	1840.5	30625
	6	260	.15	6.15	1839	3060
350 V	0	373	6.34	6.34	2364.8	356100
	1.55	343	4.67	6.22	2144.3	35675
	3.12	334	3.12	6.24	2134.1	35650
	4.65	323	1.55	6.2	2044.5	35625
	5.99	306	.15	6.14	2142.4	3560
400 V	0	426	6.34	6.34	2700.8	406100
	1.56	392	4.69	6.25	2462.5	40675
	3.15	385	3.15	6.3	2472.8	40650
	4.67	376	1.56	6.23	2454.6	40625

3.3.3. Plume Divergence

The sweeps taken by the Faraday probe with 350 V on the anode are plotted in Figure 3-8. Several observations can be immediately made from these data: the ion current density is dependent on propellant mass flow in most cases and the level of discharge electron current on the shims, and that the thrust vector appears to change slightly as the discharge current is shifted between the main anode and the shims.

The first observation is that the collected ion current density is directly affected by the propellant mass flow in the thruster; in the majority of cases the current density increased with propellant mass flow. This was an expected change, as higher propellant flows should result in more ion production and thus more ion current in the plume of the thruster. An anomalous result is seen in the data when 300 V was on the anode, however. In the 25% and <5% levels of discharge electron heating on the shims, the peak current density with 5 mg/s of mass flow was on the order of, or smaller than, the peak density at 4 mg/s. This coincides with some of the performance measurements taken of the thruster at these operating points. A beam with poor focusing, as appears to be the case in the 305 set of operating conditions, would exhibit lower thrust, specific impulse, and efficiency than a thruster with a well-collimated beam.

It also can be seen from the data that the ion current density is dependent on the shim voltage. At all combinations of anode voltage and mass flow, the peak ion current density increased with increasing shim voltage, and thus increasing levels of discharge electron heating on the shims.

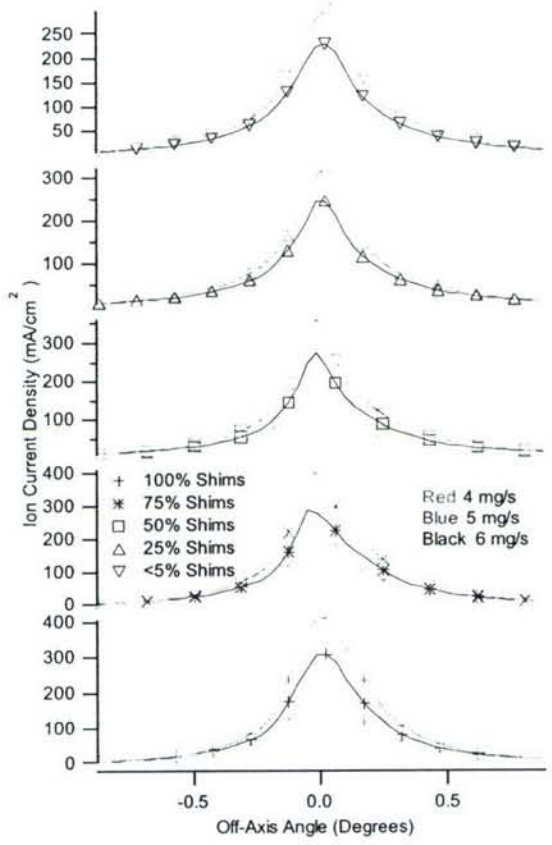


Figure 3-8: Beam Profiles with 350 V on the anode at all mass flows and levels of discharge current heating.

Determination of the beam divergence can be accomplished through integration of the ion current density. Using a point along the axis and at the exit plane of the thruster as the zero point, an integration in spherical coordinates can be performed, which will yield the total beam current. Integration was performed using the following equation:

$$I = \int_{-\theta_m}^{\theta_m} \int_0^{\pi} J_i r^2 \sin\Theta d\varphi d\Theta$$

The bound on the integration in Θ is due to the current measurements being taken at up to two equal angles off-axis of the thruster. Due to the double-sided nature of the integration in Θ, the integration in φ was performed between zero and π. J_i is only a function of Θ, so the double integral can be simplified to a single integral:

$$I = \pi r^2 \int_{-\theta_m}^{\theta_m} J_i \sin\Theta d\Theta$$

As both Θ and J_i are discrete, the integral was solved numerically using the trapezoid method. The beam divergence was calculated by determining the half-angle required to include 90% of the total beam current. The results of this calculation are plotted in Figure 3-9. In nearly all of the data traces the beam divergence was lowest when all discharge electron heating was on the shims and highest when 25% of the discharge heating was on the shims. There were three notable discrepancies to this; in the 404-, 406-, and 306-set of operating conditions the divergence remained the same or slightly decreased as the discharge electron heating was shifted from 25%

on the shims to <5% on the shims. Additionally, the 404-set of operating conditions showed a much higher than expected result at 100% of the discharge heating on the shims. The beam divergence also appeared to be dependent on thruster voltage and propellant mass flow. Increasing voltage and mass flow both appeared to contribute to a lower beam divergence.

Analysis of the calculated beam divergence through analysis of variance showed that as expected from the data, all three experimental factors contributed to the beam divergence, with P-values ranging from 3.5×10^{-13} to 3.7×10^{-12}. Additionally, the width of the 95% confidence interval was 1.01 degrees, roughly one quarter of the total change in beam divergence caused by the shift of current from the shims to the main anode. An interesting result, however, is that the effect from the level of discharge current sharing on the shims has the most significant impact on the beam divergence. This can be seen in the plot of beam divergence; the shim voltage (and thus, amount of discharge heating on the shims) caused beam divergence to change by up to four degrees, while voltage or mass flow only accounted for two degrees at most. Thus the shims appear to have a focusing effect, forcing the ion beam to be more collimated with high levels of discharge heating on the shims. This is a significant change in beam divergence, as much as a 10% reduction as discharge electron heating is shifted from the main anode to the shims, so use of shim electrodes in a configuration similar to that examined here will reduce the beam divergence in potential flight applications. This is not completely unexpected, as the Princeton Plasma Physics Laboratory saw similar results with the addition of segmented electrodes for beam divergence control.[2,3,4] However, as the nature of the operation of a bismuth thruster requires that the level of discharge electron heating be constantly modified, and also that it will be very rare that all discharge electron heating is on the shims, use of the highest value of beam divergence seen should be used in any spacecraft interaction analysis, as the thruster will likely need to operate at that point at some time during a mission.

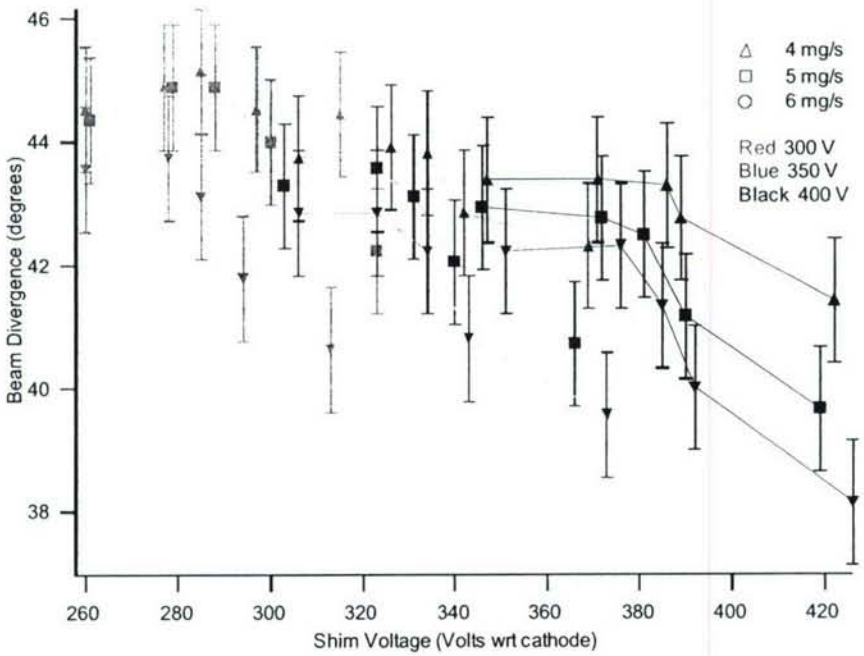


Figure 3-9: Beam divergence as a function of all three experimental factors.

3.3.4. Ion Energy Characterization

Ion energy was measured using a retarding potential analyzer. The plasma- and secondary-electron repellers in the probe were biased 10 V below ground to ensure no electrons from either the plasma or from secondary electron emission could affect the measurements. The entrance grid was physically connected to the probe shell and allowed to float, thus screening out the high voltages inside the probe, and minimizing the effect on the plasma. The ion repeller voltage was swept between 0 and up to 600 V at roughly 0.5 Hz. The data were averaged via an oscilloscope up to eight times before output to a computer, to minimize the effect of noise on the measurements.

After normalization and taking the derivative of the probe current the average ion energy was calculated. Both the most probable energy and the average energy are of interest, however, as they each can provide insight into the ion acceleration process in the thruster. A change in the most probable ion energy indicates a change in the acceleration potential at the point where the majority of ions are accelerated, while changes in the average ion energy indicate a net increase or decrease in ion acceleration potential. These are not necessarily the same; an acceleration potential structure could be produced which will accelerate most of the ions to a given energy, but produce a significant population of ions at either a higher or lower velocity than the most probable. These populations of fast or slow ions would affect the average, despite the fact that the most probable ion velocity may be the same as in another operating condition.

The derivatives of probe current as a function of ion repeller voltage for one mass flow condition (4 mg/s) is plotted in Figure 3-10. The currents were normalized to unity before differentiating, thus the ion energy distribution functions calculated are area normalized and show the trend in the ion energy distribution. Aside from the expected increase in ion energy with anode voltage (and corresponding increase in shim voltage), the ion energy showed a significant change between the condition with all current on the shims and the other levels of shim current. In all of the cases displayed, the peak of the ion energy distribution was 20-30 eV/q higher when all discharge current was on the shims than any other amount of shim current. This indicates a strong dependence on shim voltage, but only at operating conditions where the shim voltage is higher than the main anode voltage. In each of these cases, the shim voltage was approximately equal to the main anode voltage with 75% of the discharge heating on the shims, and the shim voltage was always lower than the anode voltage when the shims were accepting less than 75% of the discharge current. These data suggest that the ion acceleration is governed by the highest potential present in the thruster: Shim voltage governs at high shim voltages, and anode voltage governs at low shim voltages. Another conclusion that can be drawn is that the ion distribution function is more spread out when all of the discharge current was on the shims. The short peak of the normalized distribution with all discharge heating on the shims indicates that the ion acceleration process is more spread out at that operating condition than when the shims are accepting less of the discharge electron heating. Thus while the most probable ion energy is higher when all discharge heating is on the shims, the thruster is accelerating ions over a much wider range of energies.

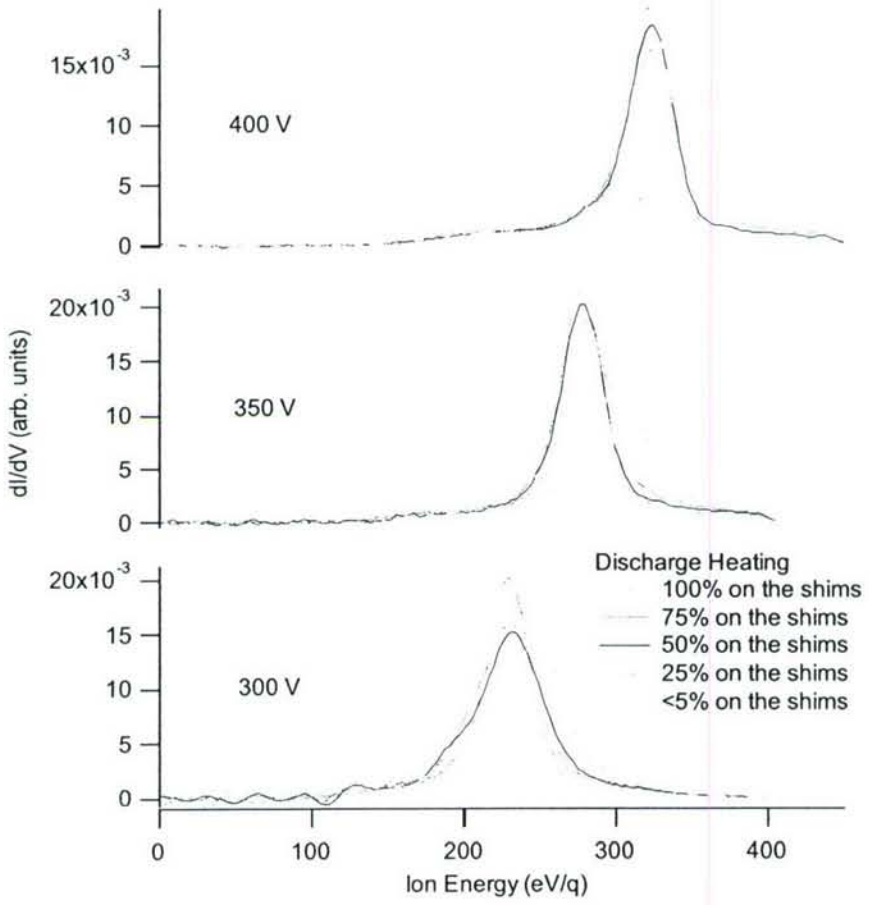


Figure 3-10: Derivatives of RPA current with at 4 mg/s of xenon, at all combinations of anode voltages and shim levels.

The most probable ion energy, as plotted for all operating conditions in Figure 3-11, verifies the strong dependence seen in **Error! Reference source not found.** on anode and shim voltages. The ion energies show an approximately 50 eV increase with each 50 V increase in anode voltage. Thus the effect of the anode voltage on the ion energy is roughly linear, with increases in anode voltage being mirrored in the most probable ion energy. The changes in ion energy as anode voltage was adjusted are expected, as alterations to the anode potential directly adjust the electric field through which the ions are accelerated. Very little change is seen in ion energy as a function of mass flow. The change in ion energy as a function of shim voltage verifies the dependence on the highest voltage in the thruster. For shim voltages above the main anode voltage, the ion energy appears to increase with shim voltage. At shim voltages at or below anode voltage, however, the ion energy becomes somewhat independent of the shim voltage; further reductions of shim potential below anode potential do not affect the ion energy. These results indicate that the highest voltage present in the thruster determines the most probable ion acceleration potential, whether that is anode or shim voltage. While it cannot determine the exact location at which the acceleration takes place, measurement of the most probable ion energy has revealed that the ion acceleration process is governed by the shim voltage in a slightly different way than the specific impulse; while specific impulse decreased with shim voltage, the ion energy appears to hit a minimum energy, dictated by the anode voltage, and remains roughly at that voltage for all operating points where the shim voltage was below anode voltage.

Application of the analysis of variance to the most probable ion energy, calculated from the ion energy distribution functions, verifies the expected dependence of ion energy on the anode and shim voltages in the thruster. The calculated P-values ranged from 2.8×10^{-40} to 1.6×10^{-3}; all well below 1%, thus verifying that each experimental factor had a significant effect on the ion energy. The 95% confidence interval has a width of 7 eV/q. This is much smaller as a fraction of the measurement than many of the other errors calculated; the error is between 2 and 3.2% of the measurement. Unlike the trends in thrust and specific impulse, the changes in ion energy with the most significant factors (anode voltage and shim level) are larger than the confidence interval; thus the anode voltage and level of discharge electron heating on the shims are both primary contributing factors to the most probable ion energy in the exhaust plume of the Hall thruster.

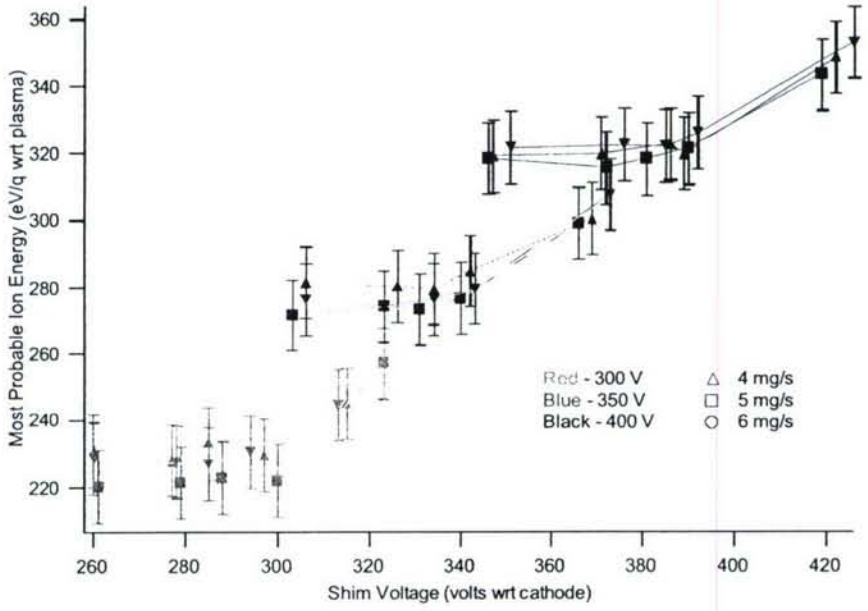


Figure 3-11: Most Probable Ion Energy as a function of all three experimental factors. Higher shim voltage indicates a higher proportion of discharge current on the shims.

3.3.5. Multiply Charged Ion Fraction

A typical set of ExB probe traces is in Figure 3-12, taken at 400 V on the anode and 4 mg/s of xenon. The ExB distributions at other operating conditions were similar. The ion velocities are not corrected for plasma potential. The exact position of the peaks of ions of different charge states is unimportant for calculation of the multiply charged ion fraction, as the peak height is the only important parameter in this determination.

Each trace in Figure 3-12 therefore shows the velocity of ions as they passed through the probe filter. Three peaks are clearly visible in each trace. The spacing between peaks indicates that the first peak is singly charged xenon, the second doubly charged xenon, and the third peak triply charged xenon. This determination can be made because the velocity of the doubly charged xenon peak is roughly 1.4 times the velocity of the singly charged xenon peak. Doubly charged xenon, when accelerated through the same acceleration potential as a singly charged ion will have

$\sqrt{2}$ (approximately 1.4) times the velocity as a singly charged xenon ion, so the peak is most likely to be doubly charged xenon. The velocity is far too high to be singly charged xenon produced and accelerated by a thruster at 400 V, and thus must be doubly charged ions. The third peak in the distribution is similarly at approximately $\sqrt{3}$ times the velocity of the singly charged peak; the expected velocity of triply charged xenon, while being too fast to be either singly or doubly charged xenon. Xenon ions of higher charge states were not characterized. Extremely weak peaks were present at very high velocities at some thruster operating points that may have been quadruple-charged xenon, however the inconsistent appearance and small size of these peaks made comparison across all thruster operating points impossible and thus were neglected. Distribution peaks at velocities corresponding to higher charge states were not seen.

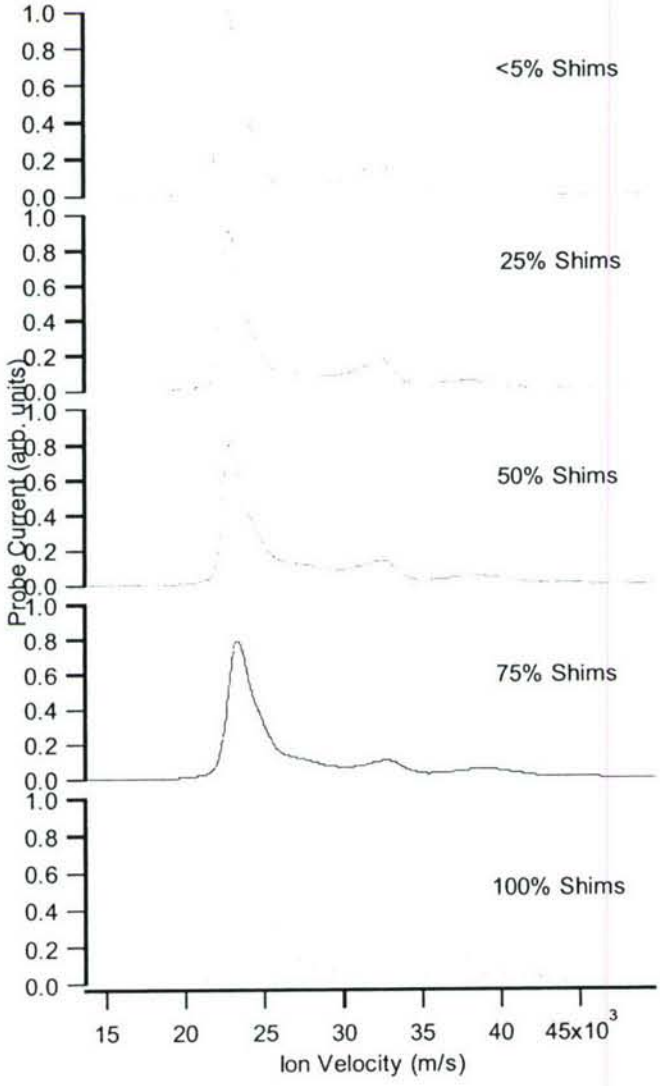


Figure 3-12: typical set of ExB probe traces taken as the level of shim current was varied. Data are for 400 V on the anode and 4 mg/s of xenon.

Analysis of the multiply charged ion fraction calculated by an ExB probe can be greatly simplified by developing an average ion charge. This is calculated from the relative density of each charge state of ions in the plasma, and allows for analysis of the entire plasma as a whole rather than as three smaller parts. The average charge was calculated using the equation:

$$\overline{q} = \sum_{i=1}^{Z} q_i F_i$$

As the highest charge state measured was triply charged ions, the value of Z is 3. The average charge at all operating points examined is in Figure 3-13. The first observation which can be made is that the charge varied very erratically with the level of discharge current on the shims.

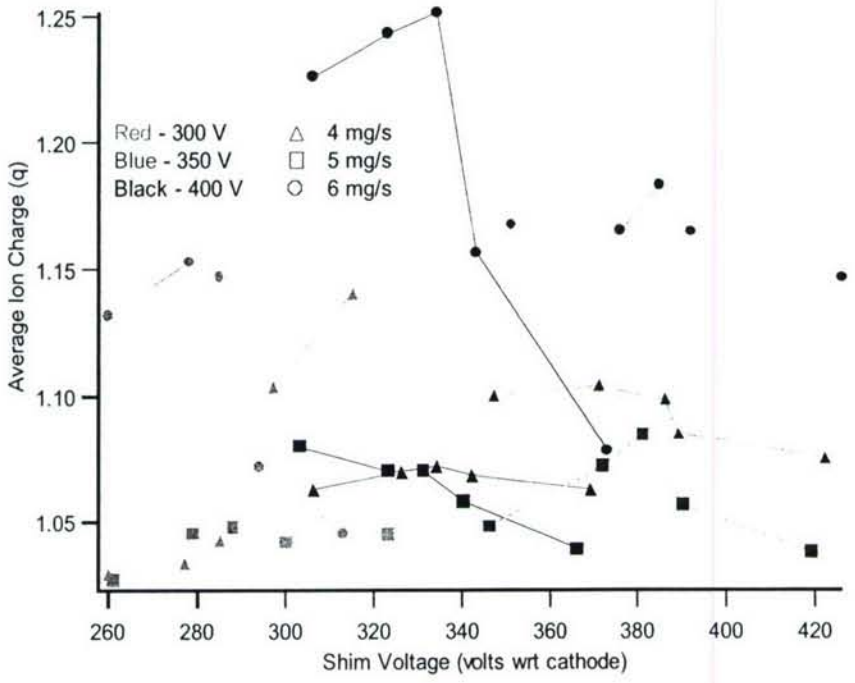


Figure 3-13: Average ion charge as a function of all three experimental factors. High shim voltage for indicates a higher fraction of discharge current heating on the shims.

Determination of the statistically significant factors in the average ion charge allows a picture to be generated of the significant factors in each charge state. The average charge is a composite measurement of all charge states, thus finding the statistically significant factors is therefore applicable to the entire population of ions and not merely to one charge state. Shim level, with a 24.5% certainty in the null hypothesis, was determined not to be a significant factor in average ion charge. Thus much the same conclusion is reached by analyzing the average ion charge as was reached by analysis of each component separately; mass flow has the largest effect on the multiply charged ion fraction, anode voltage is still significant but not to the same degree as mass flow, and shim level was not a significant factor. Using the mean squared error generated by the analysis of variance, the 95% confidence interval on the average ion charge has a width of 0.07 fundamental units of charge. This is between 5.9 and 7.2% of the calculated average ion charges.

The uncertainties calculated on the multiply charged ion fractions are very large, and complicate further analysis of other thruster parameters as a function of multiply charged ion fraction. Some of this is inherent to the measurement method; an error of a few percent of the total ion population can be several times the fraction of triply charged ions. There are some fundamental limits to the analysis method utilized, however, which limit the accuracy of an ion charge fraction measurement. The only way to truly determine the ratios of each charge state of ions is to find a function that describes the shape of the distribution function exactly. This cannot be trivially done on the data reported here, however, as the uncertainty in the ion energies allowed to pass through the ExB probe is too large. Broadening of the distribution function caused by the energy resolution error makes finding a functional fit impossible, as the function will classify some ions of a given charge state as belonging to a different charge state. Increased resolution of the probe would allow for much finer resolution of the ion population peaks, and make either a functional fit or a more accurate measurement by peak height possible.

3.4. Discussion

3.4.1. Thermal Data

In this application, the goal of using segmented anodes was to enable thermal control of the main anode for use in eventual bismuth evaporation. In each of the cases presented in Figure 3-3, a 50+ degree variation in temperature was obtained in a matter of minutes for the main anode, and in seconds for the shim electrode. In the thermal region of interest, a 50-degree swing in temperature would cause a 63% change in the bismuth evaporation rate, providing a wide range of throttleability. Moreover, at the tested power levels, the anodes are both thermally stable and well within the working temperature of the constituent materials. From these results, it is clear that using segmented anodes for thermal control is a valid approach.

Although thermal testing showed the ability to substantially vary the anode temperature, the maximum temperature achieved was well below that required for sufficient bismuth evaporation through self sustaining operation. It was previously determined that a reservoir temperature of 750°C was required but even running at 2.4 kW the main anode temperature reached a maximum 597°C. To gain the additional 150 degrees, thruster power could be further increased at the expense of thruster lifetime. Another option could be to reduce the anode face area thereby increasing the power density as well as improving thermal insulation. The thruster employed in this study had a power density of 0.5 W/mm^2 (based on anode face area) and achieved 597°C. Thermal modeling suggests that a power density of 1 W/mm^2 would be sufficient to achieve the goal of 750°C.

3.4.2. Performance Changes

The segmented-electrode thruster showed some performance changes as discharge electron heating was shifted from the shims to the main anode. Thrust and specific impulse both increased with increasing shim voltage, indicating that the shim voltage is one of the factors that determine the total acceleration voltage experienced by the beam ions. Some hypotheses can be made about the accelerating potential and location of ionization from these results. Since the most probable ion energy was only dictated by the shims when the shim voltage was higher than the anode voltage, the highest voltage in the thruster must also affect the accelerating potential.

Ionization could be happening either upstream or downstream of the shims. If the ionization is taking place upstream of the shims, there is a potential issue where an ion is created and can be accelerated towards the anode instead of out of the thruster. This could happen if ionization is taking place at the peak of the thruster potential. Ions could then fall through the potential created toward or away from the main anode. This backward acceleration would cause a large efficiency loss, as ions created and accelerated towards the anode would cost energy to create and accelerate, but provide no thrust. No large decrease in efficiency was seen, so backward acceleration of ions must not be happening in any significant quantity. Thus if ionization is taking place upstream of the shims, the potential hill inside the thruster must be such that the decrease to anode potential is very close to the anode itself. Ions thus would not be created where they could fall back towards the anode and would be accelerated out of the thruster. As shim voltage is decreased, the effect on the potential inside the discharge channel is reduced and the potential will become more dictated by the anode. Thus when the shim voltage is lower than the anode voltage, ions created upstream of the shims would be accelerated by the anode potential, not the shim potential, and show the ion energy behavior seen.

Ionization could also be taking place downstream of the shims. In this case, there is little potential for backward acceleration of ions at high shim voltages. This is because ions downstream of the shims are not at the crest of a potential hill, rather partway down a slope. Thus the newly created ions could not force their way past the shims to strike the anode, rather they would be accelerated out of the thruster. This creates a complication, however, in that the shim voltage was not the primary determining factor in ion energy at low shim voltages. If ionization is taking place downstream of the shims, then the accelerating potential downstream of the shims will be affected less by the shims and more by the main anode as shim voltage is lowered. When shim voltage was lower than the anode, then, the shims would have little to no effect on the accelerating potential. This indicates that the electron current impacting the shims has a large effect on potential, and thus as less current is diverted to the shims the accelerating potential will be affected more and more by the main anode.

The absence of a statistically significant change in efficiency as discharge electron heating was shifted from the shims to the main anode is important to future development of a shim electrode thruster. In a bismuth thruster, the discharge current will need to be constantly adjusted to maintain the anode at the proper temperature. If the efficiency was significantly lower at any of these levels of discharge current sharing, the power needs of the thruster will increase, thus increasing the size and mass of the power supply, making such a thruster system less desirable over chemical or gaseous EP systems. A change in efficiency was not seen, so the conclusion can be made that a bismuth thruster of the design described in Chapter 2 could be operated at a controlled propellant mass flow without a detrimental effect to the thruster efficiency.

A final conclusion which can be made from the performance measurements is that there is no backwards acceleration of propellant ions when the shims are at a higher voltage than the main anode. This was a concern due to the fact that when the shim voltage was higher than the anode voltage, it should have been possible for ions to be created upstream of the shims and accelerated back towards the anode. Backward acceleration can manifest in two ways, none of which were present to a significant degree in the performance measurements. First of these is a reduction in anode current due to positive ions canceling out some of the current from the negatively charged electrons impacting the anode. In the majority of thruster operating points, the current did not decrease as the shim voltage was raised above the anode voltage, rather in most cases the discharge current increased with shim voltage. The second manifestation of backward acceleration is in the performance of the thruster, especially efficiency. Any ions accelerated backwards will cost the thruster energy, both in ionization and the energy used to accelerate the ions. This will manifest as a direct efficiency loss to the thruster, as well as a reduction in thrust and specific impulse. It is unlikely that any significant quantity of ions are

being accelerated back towards the anode when the shim voltage exceeds the main anode voltage since the thruster showed higher thrust and specific impulse at high shim voltages, and efficiency did not change.

3.4.3. Plume Changes

Each of the three plasma diagnostics performed assisted in determination of the source of the performance change seen as the thruster discharge current was shifted from the main anode to the shims. Through the use of each of these diagnostic methods, a separate aspect of the thruster plume was investigated, and could be correlated with the observed performance changes.

The results of these plasma diagnostics showed that the plume changes in two significant ways as discharge current is shifted from the main anode to the shims. When all of the thruster current was attached to the shims through high shim voltage, the thruster plume was narrower and consisted of higher-energy ions. This change was seen in the plume divergence data from the Faraday probe, which showed that the thruster plume exhibited a roughly 10% lower beam divergence at high shim voltage than at low shim voltage. This reduced plume divergence should have caused an efficiency increase, as the ions accelerated closer to the thruster axis will provide more benefit (thrust) than ions accelerated perpendicular to the thrust axis to a significant degree. This expected efficiency increase was not seen, however. The efficiency of the thruster did not significantly change as the discharge current was shifted from the main anode to the shims, thus the results from the plume divergence study and the thruster performance study are in conflict. Despite the statistical calculations which say that thruster efficiency did not change significantly, the efficiencies plotted in Figure 3-7 show slight increases with shim voltage. While the increases in efficiency with shim voltage were statistically insignificant, the possibility remains that the increase was real and simply overwhelmed by the error. This conflict will require future experimentation to resolve. Duplication of the performance measurements taken here will reduce the estimated variance, and may allow for resolution of a small change in thruster efficiency with shim voltage. Plasma diagnostics inside the thruster discharge channel may also provide insight into the nature of the discharge as the shim voltage is adjusted and may explain the lack of significant efficiency changes with plume divergence.

Characterization of the ion energy showed that the ion acceleration is directly dependant on the shim voltage. Both the most probable and average ion energies were high for high shim voltage and low for low shim voltage. While the average ion energy decreased with respect to ground as the shim voltage was reduced the most probable ion energy did not. The most probable energy seemed to exhibit a large dependence on shim voltage only when the shim voltage was higher than the main anode voltage. When the shims were at a lower voltage than the main anode, the most probable ion energy remained roughly constant, and did not appear to be dependant on the shim voltage. This change in behavior indicates that the most probable ion energy is dependant on the highest voltage present in the thruster.

Ion energy has a small impact on thruster efficiency. As shown in the analysis in Appendix A, the fraction of thruster power required to ionize the propellant decreases as specific impulse increases. An increase in specific impulse (and thus ion energy) will cause a corresponding increase in efficiency. Both the average and most probable ion energies changed by approximately 10% over the range of shim voltage adjustments, which will reduce the ionization penalty to the thruster by roughly 10%. Thus the efficiency of the thruster should have been higher at high shim voltages than it was at low shim voltages. This agrees with the conclusions seen from the plume divergence characterization, that the statistically insignificant efficiency changes seen as shim voltage was increased may be real, and will require additional experimentation to establish. The ion energy characterization will benefit greatly from plasma

diagnostics inside the thruster discharge channel, as interior diagnostics may help determine why the ion energy changed.

Determination of the ion multiply charged fraction showed that there is little change in multiply charged ions as discharge current is shifted from the main anode to the shims. None of the ion fractions measured exhibited a statistically significant change as the thruster current was shifted from the main anode to the shims. While the extremely large error on these measurements complicates the determination of the multiply charged ion fraction somewhat, the lack of a change is in good agreement with the calculated thruster efficiency. An increased production rate of multiply charged ions will decrease thruster efficiency, thus the absence of a change as discharge current is beneficial to bismuth thruster operation. In this way, the multiply charged ion fractions correlate well with the observed efficiency of the thruster, in that neither changed as discharge current was shifted from the main anode to the shims.

3.4.4. Efficiency Analysis

The anode efficiency calculated from the performance measurements does not show the increase with shim voltage expected from the plume diagnostics. Both the ion energy and plume divergence diagnostics showed changes with shim voltage which should have affected the anode efficiency. The difference between the expected versus observed changes in efficiency can be calculated from the equation:

$$\eta_A = \eta_B \eta_\varepsilon \eta_i \eta_{\dot{m}} \frac{I_i}{I_d}$$

As the anode efficiency is defined here as the product of several separate efficiencies, each component can be calculated separately and combined to determine how much the efficiency should have changed due to the plume measurements. Of importance to this calculation are the beam efficiency and acceleration efficiency, η_B and η_ε. The other factors are based on parameters that were not directly measured, and thus cannot be calculated. These parameters will thus be assumed equal to one for the purposes of this analysis. Beam efficiency is a measure of collimation in the exhaust plume. It is calculated by:[24]

$$\eta_B = \frac{\int \cos^2(\theta) j(\theta) d\theta}{\int j(\theta) d\theta}$$

The acceleration efficiency is the ratio of ion energy per unit charge to discharge voltage:

$$\eta_\varepsilon = \frac{\overline{E}}{qV_d}$$

Acceleration efficiency is thus calculated from voltage and the average energy per unit charge determined by the RPA. The results of the Faraday probe sweeps provide the j required for the beam efficiency. The discharge voltage V_d used for these calculations will be the highest voltage present in the thruster. This was done because it provides an upper limit to the acceleration efficiency.

The efficiency analysis was performed on the data taken for 350 V on the anode and 5 mg/s of xenon. When all of the discharge current was on the shims, the beam efficiency was calculated to be 93%. With all of the discharge current on the main anode, the efficiency was reduced to 92%. The acceleration efficiency also decreased as shim voltage was lowered. The acceleration efficiency when all discharge current was on the shims was 92%, and the efficiency

with all current on the main anode was 90%. The product of these two efficiencies will provide an estimate of how much the thruster efficiency should have changed when discharge current was shifted from the shims to the main anode. The approximate efficiency with all current on the shims is 86%, while the efficiency with all current on the main anode was 83%. This would indicate that the anode efficiency with all of the discharge current on the anode should be 96.5% of the efficiency with all current on the shims.

Use of the calculated anode efficiency in this calculation is complicated by the large error in the measurement. None of the changes in anode efficiency were determined to be statistically significant. For the purposes of this analysis, then, the confidence interval will be ignored, and the calculated values used. The efficiency calculated from the thrust measurements showed a decrease from approximately 53% to 52% anode efficiency with the same change in shim and anode current. Thus the efficiency of the thruster with all current on the anode was approximately 98% of that when all current was on the shims. This means that the calculated change in anode efficiency was roughly half that expected by the plume divergence and ion energy. When the confidence interval on the anode efficiency is added to these calculations, the potential reduction in efficiency as the discharge current is shifted from the shims to the main anode could feasibly be equal to or larger than the change predicted by the probe diagnostics.

Several potential processes could cause the change in anode efficiency to be smaller than that predicted by the plume diagnostics. Most likely of these are increased electron mobility and a possible backward flow of ions at high shim voltages. Electron mobility is a measure of how many electrons are able to escape the magnetic field in the thruster and strike the anode. It is a significant source of efficiency loss as each electron that strikes the anode must be re-emitted by the thruster cathode, thus costing power. Ion backflow is the possible acceleration of ions towards the anode when the shims are at a high voltage. Significant amounts of ion backflow would be disastrous for thruster operation, as these ions would still cost energy to ionize, but provide no thrust and cause erosion of the anode face. Ion backflow, if present, should only affect the thruster when the shim voltage was higher than the anode voltage. For other operating conditions, with shim voltage below anode voltage, ions should not be accelerated towards the anode.

3.5. Conclusions

A segmented electrode Hall thruster was constructed and its performance and plume were characterized. The thruster was based on Aerojet BPT-2000 thruster, and retained the original design of the electromagnet and ceramic structures. The single anode was replaced with a smaller anode and a pair of ring-shaped shim electrodes, separated by ceramic spacers. The new main anode also functioned as a propellant distributor. The thruster was operated with xenon propellant. This allowed the anode temperature to be decoupled from mass flow, enabling accurate mass flows to be provided to the thruster. The thruster was operated with several performance and plasma diagnostics to determine the nature of the performance changes and to attempt to determine the source of the changes.

Segmenting the anode was shown to be viable means of obtaining thermal control. Although the ultimate temperatures sought were not obtained, the temperature variation observed lends credibility to the method of direct bismuth evaporation using discharge waste heat. Thermal modeling suggests that increasing the anode power density by reducing face area will be sufficient to achieve the desired 750°C.

The thruster showed statistically significant changes in both thrust and specific impulse as a function of shim voltage, while thruster anode efficiency did not change within the limits of the experimental error. Both the thrust and specific impulse increased with shim voltage. This

was not an entirely unexpected result; high voltages accelerate propellant ions to high velocities, thus increasing both thrust and specific impulse. The dependence on shim voltage indicates that both the main anode shim electrode voltages were driving factors in the ion exit velocity.

Thruster efficiency did not change as a function of the discharge current on the shims. This result is extremely important to future development of a segmented anode thruster as power requirements, and thus power supply size, will not change as discharge current is shifted from the shims to the main anode. This means that a segmented electrode thruster can divert current from the shims to the main anode as necessary to control the evaporation rate of a condensible propellant without negatively impacting the efficiency of the thruster.

The performance measurements thus showed that a segmented electrode Hall thruster is feasible for future development as a flight technology. Overall, the changes to thrust and specific impulse with shim voltage were small (less than 10%) and do not present a significant challenge to implementation on a spacecraft. The lack of a statistically significant change in thruster efficiency means that a thruster can be operated at all levels of shim voltage without requiring an increase in power to provide a given thrust.

Three different plasma diagnostics were utilized to attempt to determine where the changes in thruster performance come from. Thruster plume divergence, ion energy, and ion multiply charged fraction were measured, and each contributed to determining the nature of the thruster discharge and the source of the performance changes.

The thruster plume divergence was reduced by roughly 10% when the discharge current was moved from the main anode to the shims. This means that the thruster is effectively accelerating the propellant more efficiently, and less energy is being wasted accelerating propellant ions perpendicular to the thruster axis. This reduction in plume divergence can account for the increased thrust and specific impulse of the thruster. The reduced plume divergence is in disagreement with the efficiency measurements, however. The reduced plume divergence should manifest as an increase in efficiency due to less acceleration power being wasted on off-axis acceleration.

The ion energy diagnostics showed that most probable ion energy was dependant on the shim voltage. The energy showed a large decrease as current was initially shifted away from the shims, then remained relatively constant over the rest of the adjustment of discharge current back to the main anode. This change occurred over the range in which the shim voltage was higher than the main anode voltage, thus indicating that the bulk of the ions saw an accelerating potential which was dictated by the highest voltage in the thruster. At operating points where the shims were at low voltages relative to the anode, the effective acceleration was dictated by the anode and thus relatively independent of the shim voltage. At high shim voltages, the energy increased rapidly, indicating that the dominating factor in the size of the accelerating potential became the shim voltage. Thus the highest voltage present in the thruster is the dominant factor in the acceleration of the bulk of the propellant ions. Coupling these measurements with measurements inside the thruster discharge channel may assist in determination of the nature of the potential hill and the effect the shim electrodes have on the plasma inside the thruster.

Combination of the ion energy and plume divergence measurements yielded an estimate for the expected change in thruster efficiency. The thruster should have shown an approximate 4% multiplicative decrease in efficiency as the discharge current was shifted from the main anode to the shims. The thruster showed an approximately 2% multiplicative decrease in efficiency, however, indicating that there are other sources of thruster efficiency which were not characterized by this study. It is also possible that the large experimental error on the thruster efficiency measurements overwhelmed a real change in efficiency. Acquiring duplicate data to that analyzed here will greatly assist in reducing the width of the confidence interval on efficiency, and determine if the change in efficiency predicted by the plume diagnostics is present in the thruster.

Measurement of the multiply charged ion fraction showed no significant change as a function of the location of discharge current. This conclusion means that a thruster operating with a condensible propellant, using the segmented anodes for thermal control, will not produce multiply charged ions at a variable rate, and thus that the thruster can be operated at any level of discharge current sharing without an increase in the detrimental effects of multiply charged ions. The error of the probe and charge fraction measurements were very high, however, complicating the analysis of the charge fractions. While some error is to be expected when measuring the extremely small currents in the ExB probe, the resolution of the probe served to complicate analysis. Development of a model for the ions in the thruster discharge plasma that can predict and describe the data acquired by the ExB probe will greatly improve the accuracy of the probe as a plasma diagnostic for Hall thrusters.

---

[1] Pote, B. and Tedrake, R., "Performance of a High Specific Impulse Hall thruster," 27th International Electric Propulsion Conference, Pasadena, CA, 15-19, October, 2001, IEPC-01-35

[2] Fisch, N.J., Raitses, Y., et. al., "Variable Operation of Hall Thruster with Multiple Segmented Electrodes," Journal of Applied Physics Vol. 89, No. 4, p.2040, 15 February 2001

[3] Raitses, Y., Dorf, L.A., et. al., "Plume Reduction in Segmented Electrode Hall Thruster," Journal of Applied Physics Vol. 88, No. 3, p. 1263, August 2000

[4] Diamant, K.D., Pollard, J.E., et. al., "Investigation of a Segmented Electrode Hall Thruster," 40th Joint Propulsion Conference and Exhibit, Fort Lauderdale, FL, 11-14 July 2004, AIAA 2004-4098

[5] Kieckhafer, A.W., et. al., "Effect of Segmented Electrodes on the Beam Profile of a Hall Thruster," 40th Joint Propulsion Conference and Exhibit, Ft. Lauderdale FL, July 11-14, 2004, AIAA-2004-4101

[6] Kieckhafer, A.W., Massey, D.M., et. al., "Performance and Active Thermal Control of a Hall Thruster with Segmented Anodes," Journal of Propulsion and Power, Accepted for publication 02/2007

[7] Haag, T., "Design of a Thrust Stand for High Power Electric Propulsion Devices," 25th Joint Propulsion Conference and Exhibit, July 10-13, 1989, Monterey, CA, AIAA-89-2829

[8] Domonkos, M. T., Marrese, C. M., et. al., "Very Near-Field Plume Investigation of the D55," 33rd Joint Propulsion Conference, Seattle, WA, July 6-9, 1997. AIAA-97-3062

[9] Kusamoto, D., Mikami, K., and Komurasaki, K., "Exhaust Beam Profiles of Hall Thrusters,"

[10] Hagstrum, H.D., "Auger Ejection of Electrons from Tungsten by Noble Gas Ions," Physical Review vol. 96, no. 2, p.325, October 15, 1954

[11] Hutchinson, I.H. Principles of Plasma Diagnostics, Cambridge University Press, 2002, ISBN 0521803896

[12] Absalamov, S.K., et. al., "Measurement of Plasma Parameters in the Stationary Plasma Thruster (SPT-100) Plume and its Effect on Spacecraft Components," 28th Joint Propulsion Conference, 6-8 July, 1992, Nashville, TN, AIAA-1992-3156

[13] Garkusha, V., et. al., "Ion Energy Measurement of a D-55 Hall Thruster," 3rd International Conference of Spacecraft Propulsion, 10-13 October, 2000, Cannes, p. 359

[14] Marrese, C. M., Haas, J. M., Domonkos, M. T., Gallimore, A. D., Tverdoklebov, S., and Garner, C., "D-100 Performance and Plume Characteristics on Krypton," 32nd Joint Propulsion Conference, Orlando, FL, July, 1996. AIAA-96-2969

[15] Kemp, R.F., and Sellen, J.M., "Plasma Potential Measurements by Electron Emissive Probes," Review of Scientific Instruments vol. 37, no. 4, pp. 455-461, 1966.

[16] Kim, S-W, and Gallimore, A.D., "Plume Study of a 1.35-kW SPT-100 Using an ExB Probe," AIAA-99-2423

[17] Kim, S. W., Experimental Investigations of Plasma Parameters and Species-Dependent Ion Energy Distribution in the Plasma Exhaust Plume of a Hall Thruster, Ph.D. Dissertation, University of Michigan, 1999

[18] Hofer, R. R., "Development and Characterization of High-Efficiency, High-Specific Impulse Xenon Hall Thrusters," Ph.D. Dissertation, University of Michigan, 2004

[19] King, L. B., Transport-property and Mass Spectral Measurements in the Plasma Exhaust Plume of a Hall-effect Space Propulsion System, Ph.D. Dissertation, University of Michigan, 1998

[20] Manzella, D.H., "Stationary Plasma Thruster Plume Emissions," IEPC-93-097, Sept. 1993

[21] Montgomery, D.C., Design and Analysis of Experiments, John Wiley and Sons 2001, ISBN 0-471-31649-0

[22] D. King, et el "Development of the BPT Family of U.S.- Designed Hall Current Thrusters for Commercial LEO and GEO Applications" 34th AIAAIASMUSAUASEE Joint Propulsion Conference and Exhibit July 12-15, 1998 / Cleveland, OH.

[23] Hofer, R. R., "Development and Characterization of High-Efficiency, High-Specific Impulse Xenon Hall Thrusters," Ph.D. Dissertation, University of Michigan, 2004

[24] Ross, J.L., et. al., "Efficiency Analysis of a Low Discharge Voltage Hall Thruster," Journal of Propulsion and Power, submitted 06/2007

4. Bismuth Thruster Operation

4.1. Initial Results using Xe Hot Start

A unique dual-propellant anode was designed for bismuth development and testing. The anode was designed to accommodate gaseous xenon and bismuth simultaneously. The ability to run on xenon allows the thruster to achieve the high temperatures required for bismuth evaporation without the need for resistive heating. Figure 4-1 is an illustration of the anode cross section. Xenon is fed into the lower chamber where it then flows out the gas diffuser holes. Bismuth is contained in a separate chamber and is delivered to the anode via a hydrostatic reservoir external to the thruster. The bismuth vapors leave through a gas diffusing plate on the top of the anode, made from stainless-steel, which prevents liquid intrusion into the discharge chamber.

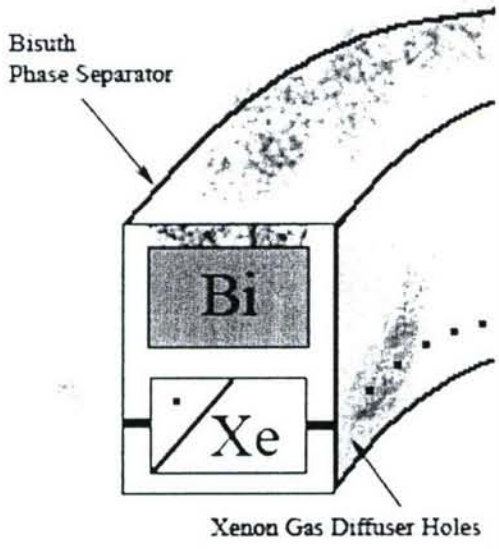


Figure 4-1. Dual-propellant anode cross section. Porous phase descriminator was constructed from stainless-steel.

The external bismuth reservoir is simply a welded stainless steel tube that is filled with bismuth prior to testing and uses hydrostatic pressure to ensure that the anode reservoir is full at all times. During operation, external resistive heating is applied to the external reservoir to ensure that the bismuth is liquid throughout the entire feed system. The power required to keep the bismuth liquid during operation was quite modest, ranging from 25 to 100 watts depending on reservoir size.

Bismuth tests were performed in the Isp Lab's one-of-a-kind Condensable Propellant Facility on the campus of Michigan Technological University. The facility is comprised of a 2-m-diameter by 4-m-long vacuum tank. Rough pumping is accomplished by a two-stage rotary oil-sealed vacuum pump with a Roots blower, capable of pumping at 400 cubic-feet-per-minute.

High vacuum is achieved using three 28,000-RPM magnetically levitated turbo-molecular pumps capable of pumping 2,000 l/sec each providing a robust, oil free vacuum. Anode and cathode xenon flow into the tank was controlled via 100 and 20 SCCM MKS mass flow controllers respectively.

In order to induce direct bismuth evaporation, the thruster was "jump-started" on xenon. Start-up results are shown in Figure 4-2. The thruster was operated on 40 SCCM of xenon at 400 volts and 4.42 amps. As the anode/bismuth reservoir heated up, the discharge current began to slowly climb indicating bismuth evaporation. The current was allowed to rise until reaching about 8 amps. By this time, current was increasing at a rate of approximately 1-2 amps per minute so xenon mass flow was reduced to keep the current in an 8 to 10 amp window. Eventually all the xenon gas flow was removed and the power supplies were reconfigured to run in constant current mode. If the discharge current began to drop (indicating evaporation was slowing), the supply automatically increased voltage to maintain the current. The increased voltage subsequently increased the power deposition to the main anode, which in turn increased the bismuth evaporation rate. The bismuth thruster ran for approximately 45 minutes in a completely self-sustaining mode before being voluntarily extinguished. When the thruster was running at 4kW and 12 amps on bismuth (no xenon except 0.3mg/sec cathode flow), the facility pressure was 8.5×10^{-6} Torr.

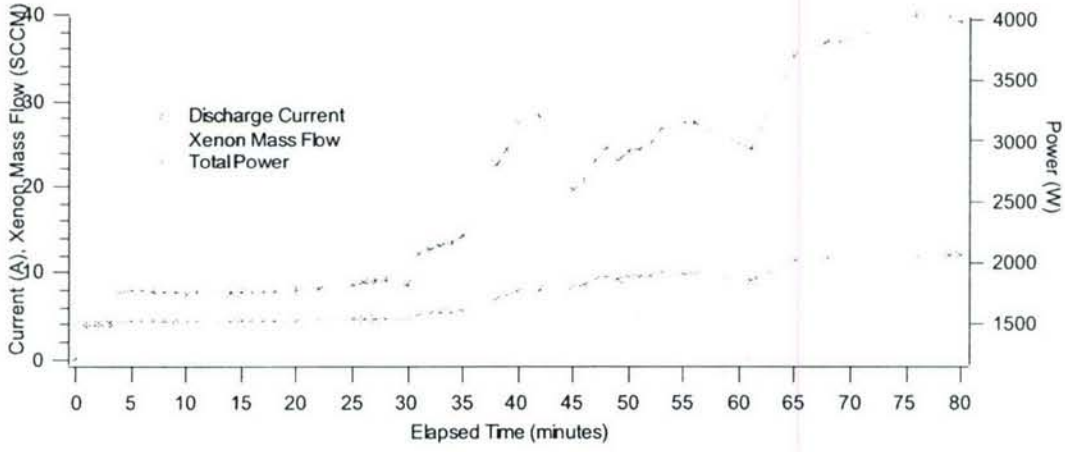


Figure 4-2. Current, power, and Xe flow rate during a "jump start" from Xe to Bi operation.

While the Xe hot-start method proved effective in inducing Bi evaporation and eventual self-sustained heating, the Bi test facility was not suitable for this method. Because the pumping speed was only 6,000 l/s (more than adequate for Bi), the tank background pressure rose into the high 10^{-4} Torr range during Xe hot start. Over multiple tests the high background pressure caused a high occurrence of arc failures within thruster power connections, feedthrus, etc. Thus, the Xe hot-start method was abandoned and replaced by a Bi-only anode equipped with resistive heaters for start-up heating.

4.2. Resistively Heated Vaporizer Design

The most critical element in the direct evaporation configuration is the vaporizer. On a basic level, the vaporizer is simply a device to separate the phases of the bismuth; liquid on one side, gas on the other. Geometric as well as material characteristics will determine how effectively the bismuth delivery system performs.

The liquid bismuth-porous vaporizer interactions are governed by very simple interfacial engineering principals. Figure 4-3 illustrates the governing forces in the case of a non-wetting liquid impinging on a capillary. A liquid is defined as non-wetting if the angle θ between the solid and the liquid is greater than 90°. Figure 4-4 is a composite image illustrating bismuth contact angles on different substrates. Since contact angles are a synthesis of properties of each of the constitute materials involved in the interface each configuration must be determined experimentally. If a non-wetting liquid is placed in contact with a capillary the intrinsic surface tension force $\mathbf{F}_{ST}$, works to counteract the applied pressure force $\mathbf{F}_P$ to retard the liquid from entering the capillary. A trivial derivation reveals that the surface tension pressure can be expressed as

$$P_{ST} = \frac{2\gamma}{r}\cos\theta$$

where γ is the surface tension and r is the radius of the capillary. From this relation it is clear that so long as P_{ST} is greater than the applied pressure P_P the liquid will not flow through the capillary.

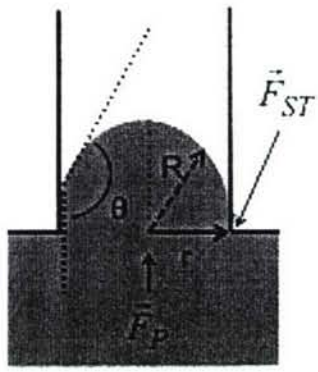


Figure 4-3. Balance of forces in response to a non-wetting fluid interacting with a capillary.

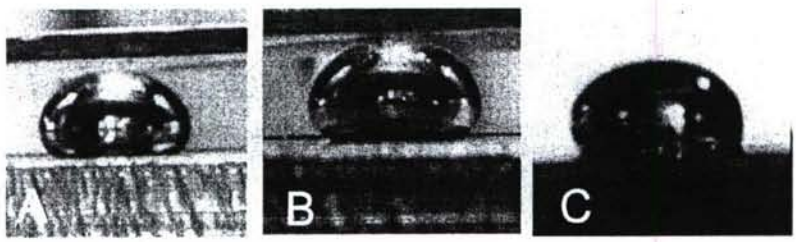


Figure 4-4. Bismuth wetting tests on stainless steel (A), molybdenum (B) and tungsten (C) substrates. In all cases the contact angle exceeds 90 therefore bismuth is non-wetting on these materials.

To extend this relation to a porous vaporizer we make a simplifying assumption that each pore behaves like a capillary of similar size. At the liquid/porous surface interface, the bismuth liquid is now pinned to one side of the vaporizer and prevented from passing through the pores. A subtle yet critical aspect of the surface tension pinning back the liquid is that a bismuth "free surface" is created allowing evaporation to commence at sufficiently high temperatures. As detailed in Ref. 4, the inherent impact of electrons into the anode will provide the heat required to evaporate the bismuth. Figure 4-5 illustrates the combined concept.

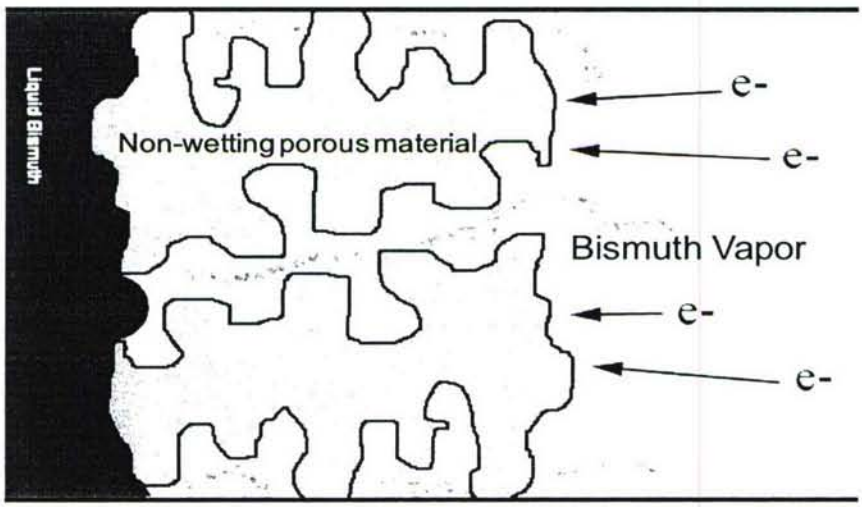


Figure 4-5. Model of liquid bismuth-porous plate interface with electron heating. Surface tension prevents the liquid from flowing through the pore yet gives a free surface for evaporation.

To verify the assumption that a piece of porous material with a given average pore size behaves like a similarly configured array of capillaries a simple test was devised and is illustrated in Figure 4-6. A stainless-steel porous disc was hermetically welded onto the bottom of a tube which served as the bismuth reservoir. Resistive heaters were wrapped around the tube so the temperature of the tube could be varied. To control the pressure with which the liquid bismuth was impinging upon the porous plate an argon gas feed line was connected to the top of the tube. The applied gas pressure was then increased until liquid bismuth was observed to be flowing through the porous plate. The results of testing two different pore sizes are shown in Table 4-1.

Table 4-1. Hydrostatic extrusion test results.

Hydrostatic extrusion test results			
Manufacturer Specified Pore Size	Theoretical Extrusion Pressure	Measured Extrusion Pressure	Effective Pore Size
0.5 μm	1,006 kPa	254 kPa	1.98 μm
10 μm	50.3 kPa	23 kPa	22 μm

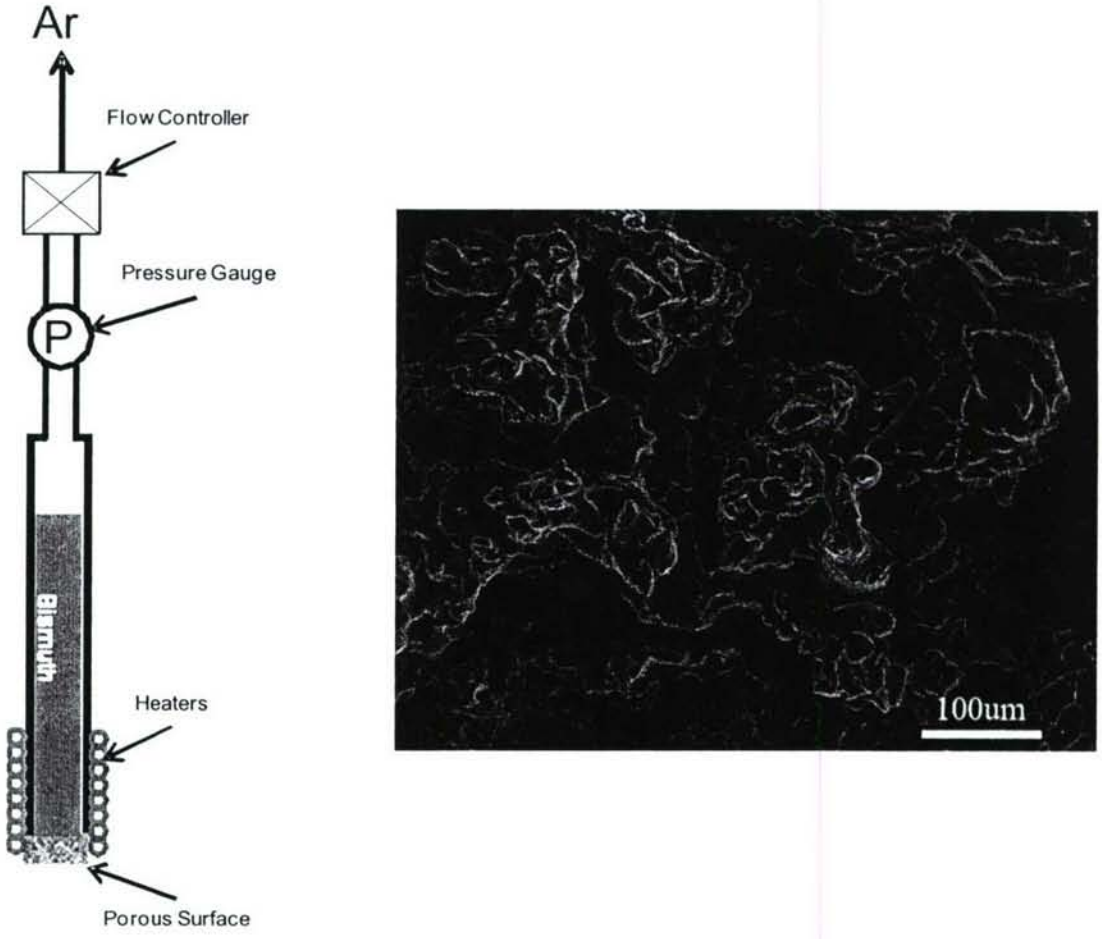


Figure 4-6. Extrusion test set-up (left). Electron micrograph of a 10-mm commercially sintered stainless-steel plate showing the statistical variation of pore size (right).

From these results several conclusions can be made. First, bismuth extrusion will initiate at the largest pore in the interface. A scanning electron micrograph of a commercially supplied plate of 10-μm porous stainless steel which shows the ambiguity of the pore size definition is shown in Figure 4-6. Due to the kinetics of sintering, the pore size is a statistical distribution rather than a fixed value. Second, results dictate that care must be taken to ensure the hydrostatic pressure of the bismuth does not approach the extrusion threshold pressure as the hydrostatic pressure on the bottom of the anode face will increase by 0.96 kPa for every centimeter of bismuth pressure head. Third, the capillary approximation does indeed provide a satisfactory estimate of extrusion pressure with the caveat that the largest pore in the plate will determine when extrusion begins. Finally, although not included in the table, the temperature of the porous plate was varied from 300°C to 1000°C with no conclusive trend in measured extrusion pressures indicating thermal effects do not appear to be a significant factor.

4.3. Porous Vaporizer Performance

Several stainless steel anodes with 0.5-μm and 10-μm size vaporizer pores were constructed and integrated into a thruster. Stainless steel was initially selected as the vaporizer material due to mature commercial availability of a wide range of pore sizes and plate thicknesses choices. The vaporizer was hermetically attached to the stainless steel anode via precision electron beam welding. Figure 4-7 is a photo of an anode laying vaporizer side face up. The left tube is connected to a larger bismuth reservoir and the longer right side tube is used as a freezing valve to allow the anode to be drained after use thus preventing potential damage cause by bismuth's 3.3% freezing expansion.

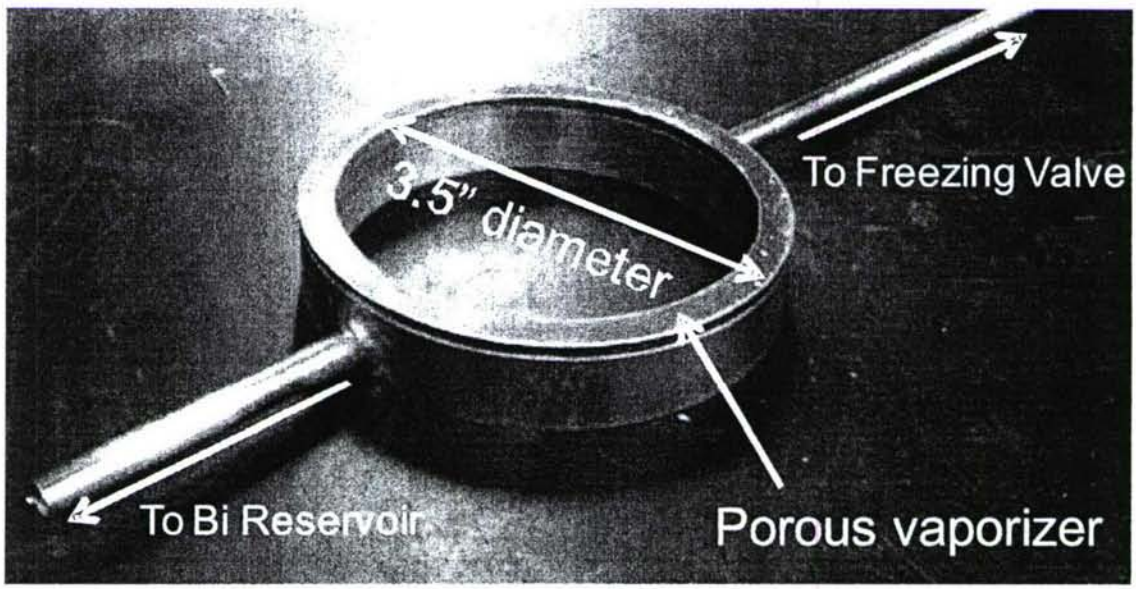


Figure 4-7. Photo of an anode laying vaporizer-side up.

The initial flow of bismuth vapors in the discharge was created by using a rhenium-doped tungsten heater that is integrated with the anode. Once there was sufficient bismuth flow to self-sustain a discharge through plasma heating of the anode face, the anode heaters were turned off. An image of the Bi operating at 2 kW is shown in Figure 4-8. Figure 4-9 is a plot of a typical extended-duration bismuth thruster test.

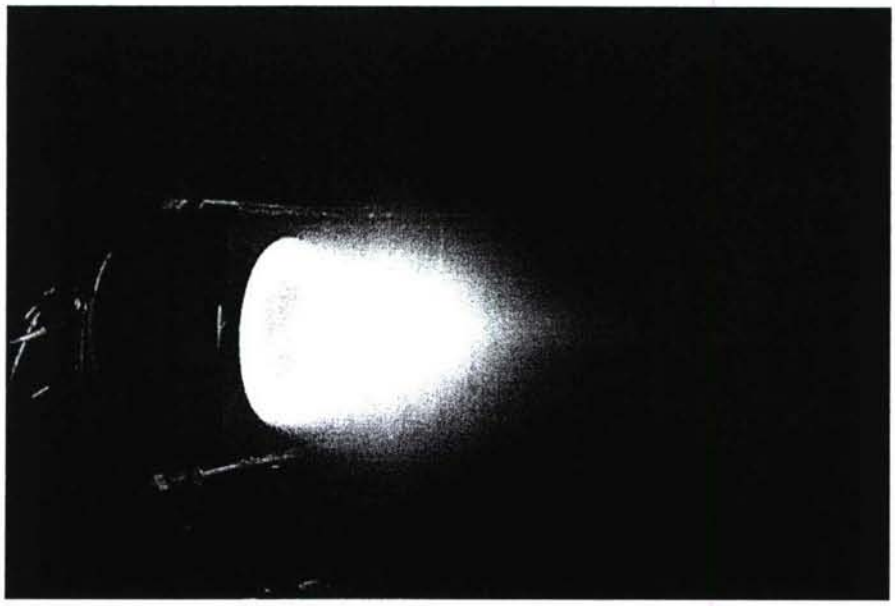


Figure 4-8. Photograph showing 2-kW bismuth thruster operating.

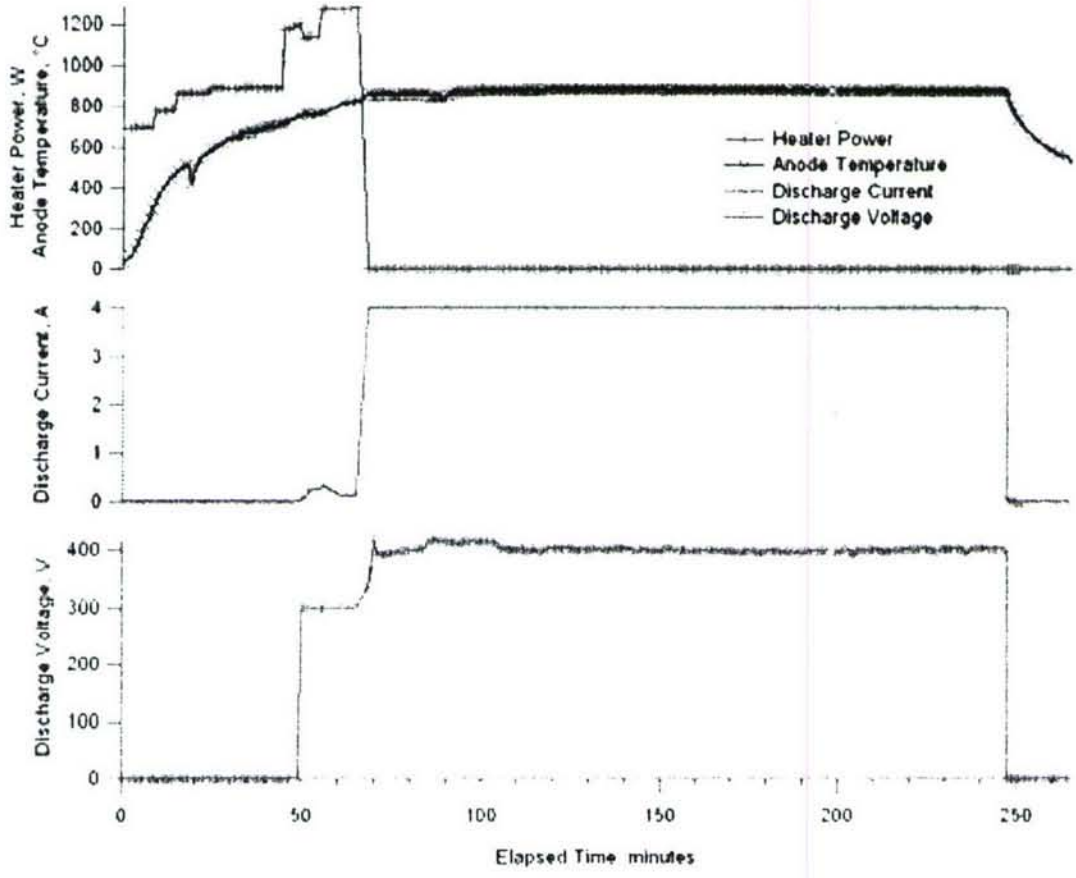


Figure 4-9 – Plot of a typical extended duration testing. After the initial warm up and transient period, steady state operation ensues.

The initial anode warm-up to approximately 800°C requires about an hour. When the thruster can maintain a self-sustaining discharge, the anode power supply is configured to supply a constant current while allowing the voltage to rise or fall to satisfy the current requirement. This type of open-loop current control displayed surprising stability, with the discharge voltage remaining constant within +,- 5 V. While the details of this fortuitous stability are somewhat unknown, the physical mechanism can be understood qualitatively by analyzing the evaporation dynamics coupled with the I-V characteristic of a HET discharge. Consider the representative I-V behavior shown in Figure 4-10 for two different values of mass flow. For constant current operation, if the mass flow increases the discharge voltage necessarily decreases from V_2 to V_1 as the thruster transitions to the higher I-V curve. This decrease in voltage, with current constant, reduces the power deposited into the anode face and, hence, reduces the bismuth evaporation rate. The same stabilizing effect would happen for a decrease in mass flow – the overall power would increase and would tend to restore the mass flow to its design value. The effect is then to correct thermal excursions away from the thruster "set point," which is determined through thermal design of the device and the geometry of the vaporizer.

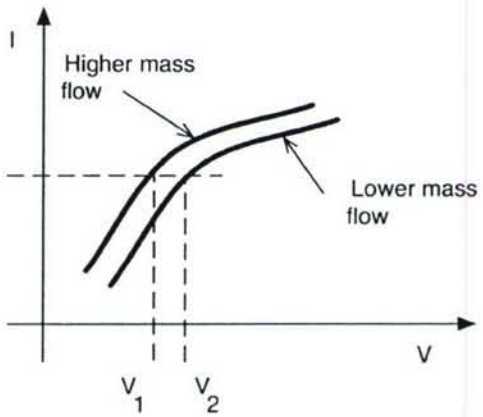


Figure 4-10 – I-V characteristics for typical HET at different mass flow rates illustrating how discharge voltage compensates for varying mass flows.

While operating in a steady state with thruster discharge voltage at 383 volts and discharge current at 4.5 amps (1.7 kW) RPA and Faraday probe data were taken in the plume. Figure 4-11 shows the accelerated ion characteristics 500 mm downstream from the thruster exit plane on centerline. The expected accelerating voltage of the ions is approximately 360 volts indicating the thruster is operating as an effective ion accelerator. Figure 4-12 is a Faraday probe sweep of the exhausted plume at 250 mm downstream from the thruster exit plane. It is apparent that the beam being exhausted is focused and quite symmetric.

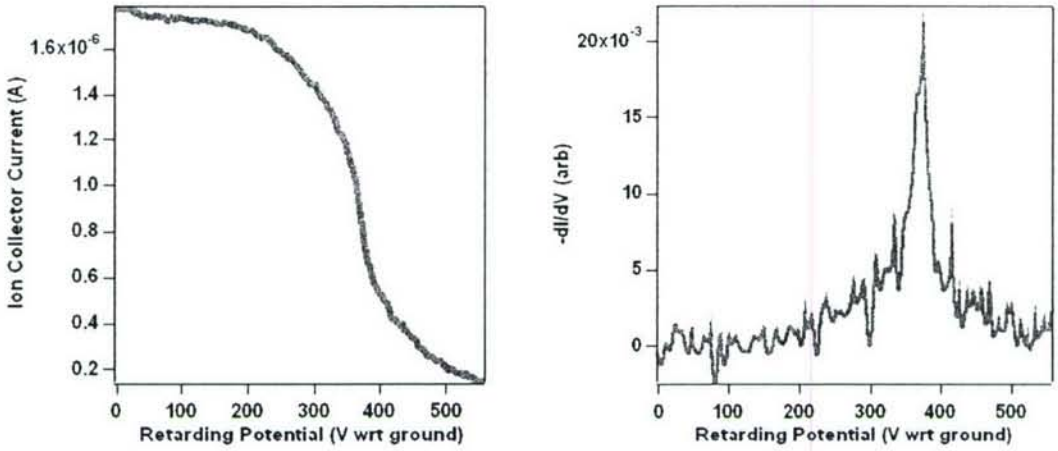


Figure 4-11 – RPA data taken at 500 mm down stream of the thruster exit plane on centerline. The expected energy of the exhausted ions is approximately 360 volts.

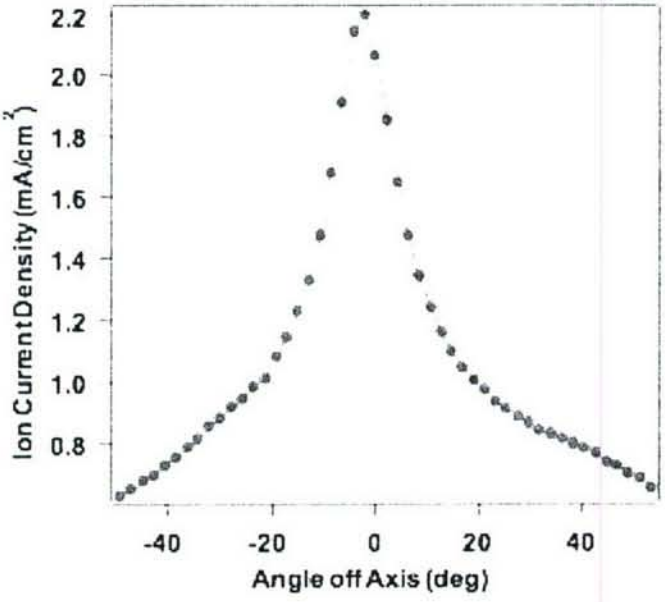


Figure 4-12 – Faraday probe sweep of the exhaust plume taken at 250 mm showing a focused beam.

Since the evaporation rate of bismuth is strictly a function of temperature, it was important to examine the face of the vaporizer to ensure a uniform temperature distribution. By pointing the thruster directly at a thermal imaging camera the temperature of not only the vaporizer but the magnetic circuit were measured. Figure 4-13 shows the results. The vaporizer face temperature is a uniform 750°C throughout and constituent magnetic circuit parts are well below their Curie point. Using the vaporizer face temperature and geometry it is estimated that the mass flow rate was about 5 mg/sec.[5]

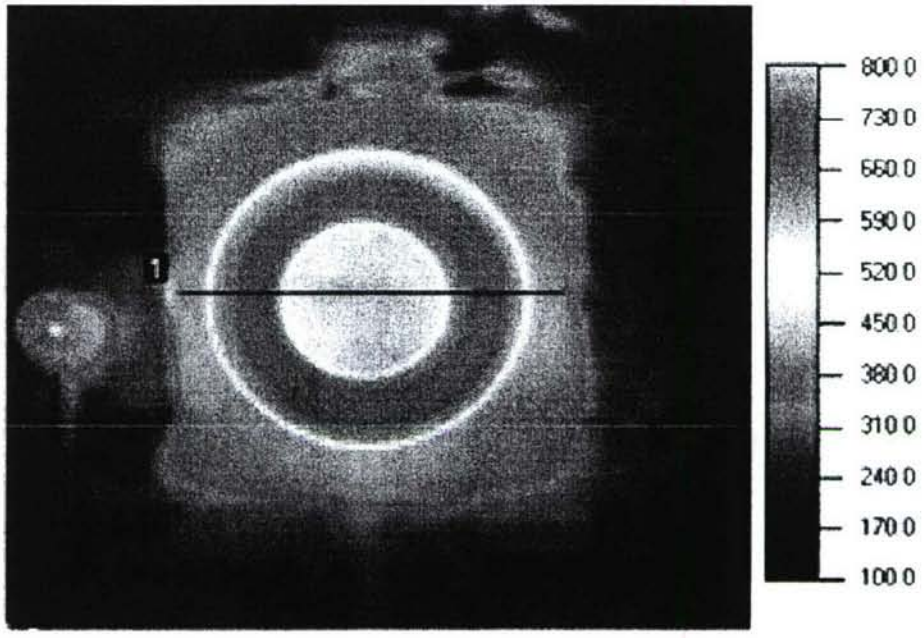


Figure 4-13 – Thermal image of the thruster taken immediately after an extended duration test. Vaporizer face temperature is uniform and the magnetic circuit is below the Curie point.

4.4. Thermal Failure of the Stainless-Steel Vaporizer

While thermal imaging and an analytical evaporation analysis indicated an expected mass flow of 5 mg/s, pre- and post-test examination indicated that mass flow rates though the vaporizer were lower. At the 1.6 kW level, the measured change in anode mass divided out over the elapsed run time yielded a mass flow rate of 1.185 mg/sec. The actual vs. theoretical discrepancy is likely due to initial over-estimation of the bismuth free surface area. Other operating points yielded similar results. Successive tests were focused on increasing the vaporizer temperature and, hence, the Bi mass flow rate.

In order to achieve the higher temperatures required, the discharge current was increased from 4.5 amps to 6.67 amps and the voltage was allowed to rise as high as 500 volts (3.3 kW). After the usual warm up period the discharge was initiated with early promising results. However, after only 10-20 minutes of self-sustaining operation bright spots would begin appear on the vaporizer face. If the thruster was allowed to continue to run with the spots, certain parts of the anode would begin to cool off and the entire discharge would begin to attach to a specific region on the anode, typically the bottom portion. Figure 4-14 is a photo of a vaporizer experiencing such a situation. On the upper portion of the vaporizer the plasma is so sparse that the glowing anode can be clearly seen whereas the bottom portion is completely obscured by a dense, bright plasma. Post test inspection of the discharge chamber revealed that at some point during operation or cool-down liquid bismuth had penetrated the vaporizer and accumulated in the bottom of the discharge chamber.

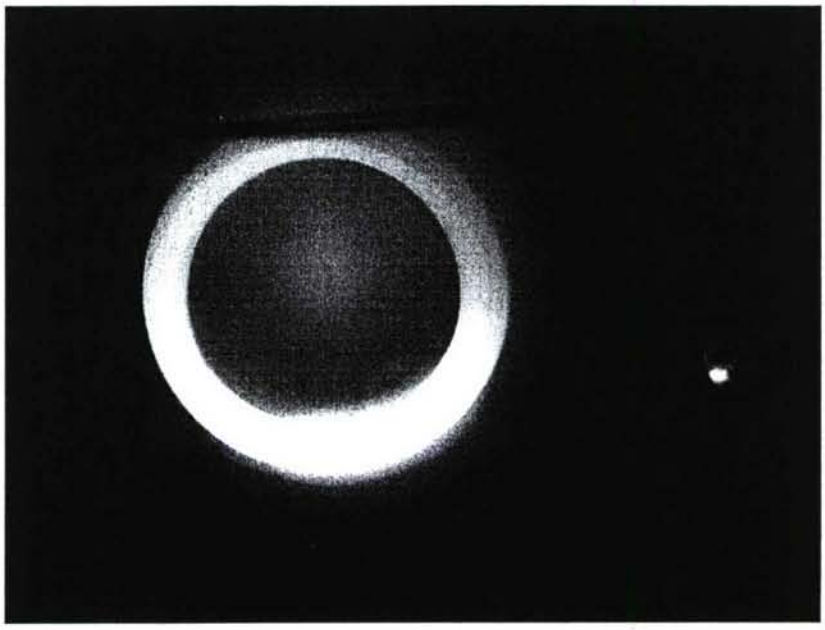


Figure 4-14 – Vaporizer during the early stages of bismuth intrusion into the discharge chamber.

After the bismuth leakage phenomena occurred several times it was clear that an underlying physical process was changing the structure of the vaporizer. After some amount of investigation it was concluded that the elevated temperatures required for higher mass flow rates were actually causing the vaporizer to continue to sinter which can certainly occur well below the melting point of the bulk material. Ordinarily sintering would result in a continued reduction of pore size but the drastically uneven hydrostatic pressure created by the bismuth was causing the pore structure to change. Undoubtedly some pores shrunk as expected but others were enlarged which eventually led to the tiny bright spots that, if left unchecked, would grow into a hole. The only recourse to fix this problem was to move to more thermally durable materials.

4.5. Porous Molybdenum Vaporizer

Molybdenum was chosen as the vaporizer material for further thruster development for several reasons. The 2623°C melting point was very attractive and the widespread availability and machinability of the material ensured this was indeed a practical choice. The only drawback of using a refractory metal as opposed to titanium or an exotic steel alloy was the lack of a commercial supplier for the requisite 3.75" porous plate. The fabrication process itself is not without precedent[1,2,3,4,5] though parts larger than the millimeter scale were not produced.

After some research it was determined that the porous molybdenum plate could be fabricated on MTU's campus using existing facilities. Following the procedures laid out in Ref 8, commercially available 1-5 μm molybdenum powder was used to obtain an average pore size of 2 μm. Approximately 72 grams of molybdenum powder was hydraulically pressed with 138 tons in a 3.75" die corresponding to a pressure of 25,000 psi. Two percent by weight stearic acid was milled with the molybdenum powder before pressing to enhance strength of the post-pressed disc. The final product was designed to be 1/16 of an inch thick thereby allowing for easy attachment to a molybdenum anode body.

The sintering process evolved over many temperatures and sintering conditions in order obtain the strongest, most uniform disc possible. Previous porous metallurgy with refractory metals was done under a reducing hydrogen environment. This was attempted but led to sub-optimal results due to the comparatively large size of the disc required. Sintering under an oxidizing environment was precluded by molybdenum forming a volatile oxide at temperatures about 600°C.[6,7] The final solution was to sinter the disc under high vacuum conditions.

Using existing vacuum facilities, a high-temperature refractory furnace was installed in the vacuum chamber. The pressed disc was placed upon a high purity alumina plate. The stearic acid binder boils off at 383°C leaving a very fragile pure molybdenum disc. Once the flatness of the disc was verified, the chamber was evacuated to high vacuum using three 2200 L/sec turbo-molecular pumps. When high vacuum was achieved, the furnace temperature was increased at 5°/min until the 1100°C sinter temperature was reached. This temperature was held constant initially for 4 hours but was eventually extended to 20 hours to ensure the late stage sintering was complete. This increase in duration lead to a significant increase in mechanical strength.

Representative results of the sintering process are presented in Figure 4-15, Figure 4-16 and Figure 4-17. Figure 4-15 is a 600x magnification of the sample interior taken along a fracture. The absence of a clear fracture plane speaks to the homogeneity of the sample and the rough break confirms that porosity has been maintained.

Figure 4-16 is higher magnification image that can be used to estimate the average pore size. At first glance it may appear that the pores have been closed but that is merely an artifact of the exceptional focal depth of a scanning electron microscope. Ignoring the background, the distance between the largest particles is the pore spacing. Like a jar of marbles, this arrangement continues throughout the sample.

Figure 4-17 is a very high-magnification image of the sample. From this image it can be definitively established that the grain boundaries of the powder have merged accounting for the substantial increase in strength. This result was not nearly as pronounced in shorter duration sintering process.

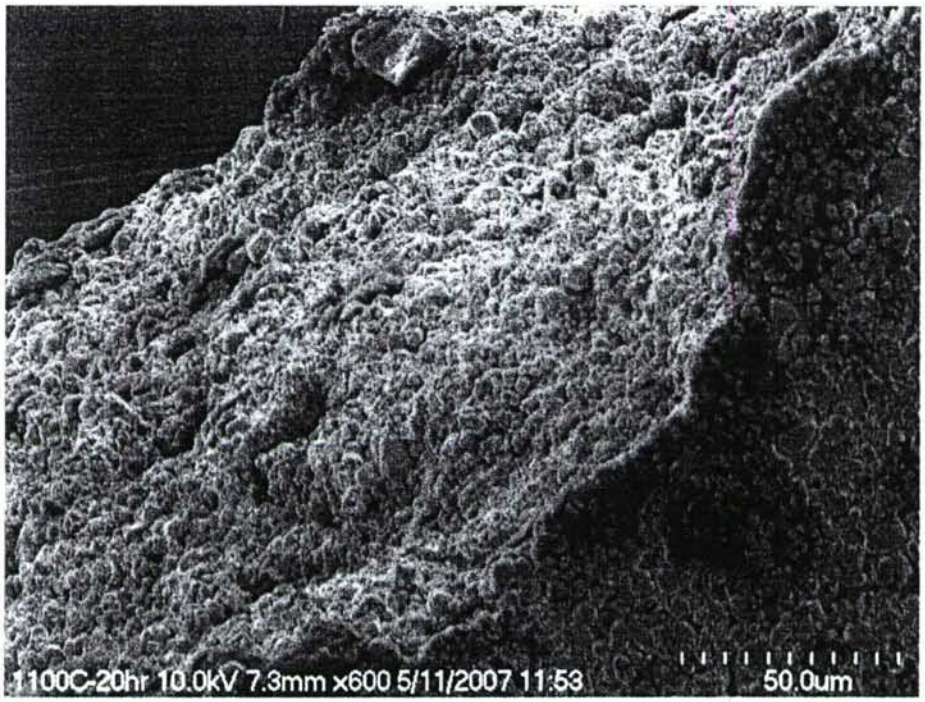


Figure 4-15 – FESEM micrograph at 600x showing some of the bulk features of the sintered molybdenum. This sample was sintered for 20 hours at 1100°C under high vacuum.

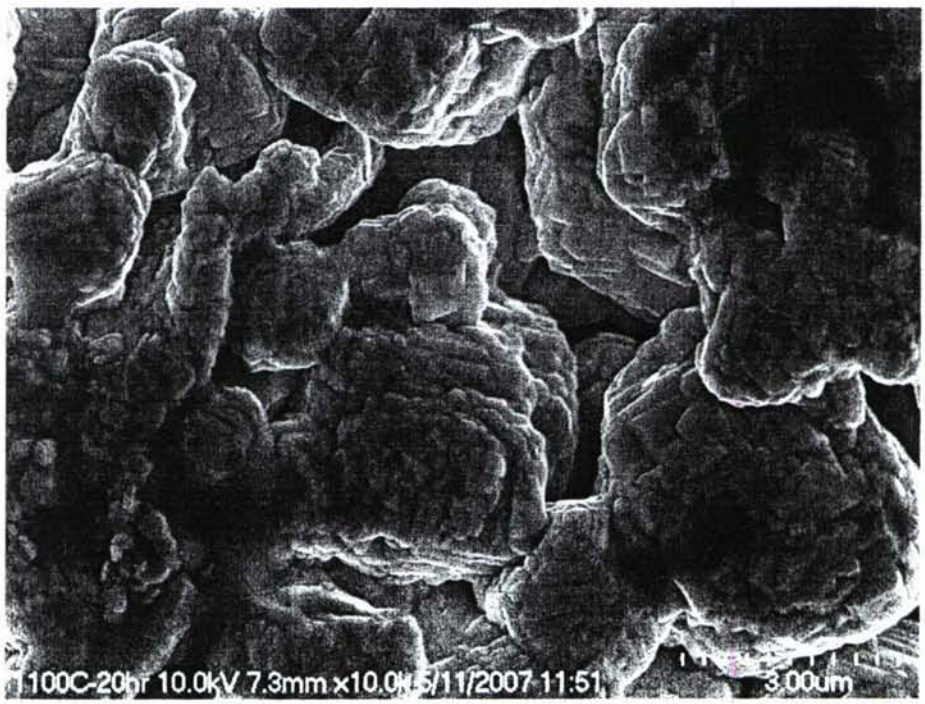


Figure 4-16 – FESEM micrograph of a representative sintered molybdenum disc at 1000x magnification. The apparent rough features of the sample indicates that late stage sintering is complete and grain growth of individual particles has occurred. This sample was sintered for 20 hours at 1100°C under high vacuum.



Figure 4-17 - FESEM micrograph of a representative sintered molybdenum disc at 40,000x magnification. The inter-particle grain boundaries are almost indistinguishable from the grains grown on the individual particles. This sample was sintered for 20 hours at 1100°C under high vacuum.

The completed discs were then cut to the appropriate shape using a 100,000 psi waterjet. Due to the brittle nature, conventional machining was not possible as clamping forces tend to break the discs. Figure 4-18 is an image of the discs cut to a suitable size for use as a bismuth vaporizer.

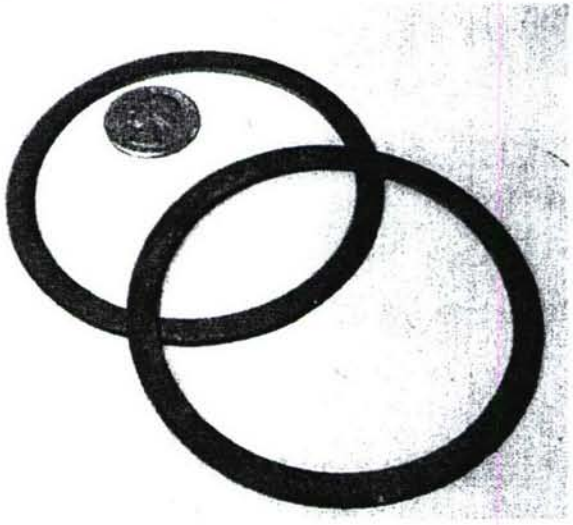


Figure 4-18 – Completed porous molybdenum vaporizer faces ready for electron beam welding.

4.6. Conclusions

Using intrinsic surface tension forces to restrict liquid bismuth flow through a porous interface is a pivotal design feature of a bismuth vaporizer. The free surface created by the interface allows bismuth to evaporate at a predictable temperature-dependent rate.

The use of stainless steel as a vaporizer is not recommended. The high temperatures necessitated by the vaporization system exceed the thermal capabilities of stainless steel. Low-power extended-duration operation is possible but the material invariably fails as temperatures and therefore mass flow rates increase. Thruster operation demonstrated a surprising stability when the discharge was configured for constant-current control. The combination of discharge current-voltage characteristic coupled with the evaporation dynamics, inducing a self-stabilizing mass-flow.

To enhance the thermal durability of the vaporizer, stainless steel was replaced with molybdenum. Through an iterative process, usable and reproducible porous molybdenum vaporizer faces have been fabricated in the sizes required for HET integration.

Unfortunately, at the time of preparation of this final report results were unavailable for Bi thruster performance with sintered Mo vaporizer.

---

[1] Kerslake, W.R., "Design and Test of Porous-Tungsten Mercury Vaporizers", AIAA 72-484, 9th Electric Propulsion Conference, Bethesda, MD, 1972.

[2] Pye, J.W. "Component Development for a 10-cm Mercury Ion Thruster", J. Spacecraft Vol 10, No. 2, 1973.

[3] Saunders, N., "Experimental Method of Producing Porous Tungsten for Ion Rocket Engines", NASA Technical Note D-864, 1961.

[4] Panichkina, V.V., et al, "Fracture Characteristics of Sintered Porous Molybdenum", Soviet Powder Metallurgy and Metal Ceramics, Vol 12, No. 24, 1974.

[5] Pustogarov, A.V., et al, "High Temperature Properties of Porous Tungsten and Molybednum", Soviet Powder Metallurgy and Metal Ceramics, Vol 14, No. 10, 1982.

[6] L.B. Pfeil, J. Inst. Metals 171, 501 (1929).

[7] A.D. Smigelskas, E.O. Kirkendall, Transactions AIME 171, 130 (1947).

5. Bismuth Cathode Development

5.1. Nomenclature

A = cathode orifice area (m^2)
k = Boltzmann constant ($m^2 \cdot kg/s^2 \cdot K$)
m = atomic mass (kg)
$\dot{m}$ = mass flow rate (kg/s)
P_v = vapor pressure (Pa)
T = temperature (K)

5.2. Introduction

The encouraging results of the bismuth thruster motivated a study to examine the feasibility of an all-bismuth system using a bismuth cathode. In addition to all of the physical and economical gains, it would be advantageous to incorporate a bismuth cathode to eliminate the need for multiple propellant supplies on an eventual flight unit. In the summer of 2005 a functioning prototype bismuth cathode was developed and a limited number of operating characteristics were reported.[1] The primary goals of the research stated here were to evaluate the operating characteristics of a bismuth LaB_6 cathode at different mass flow rates, compare bismuth data with xenon and krypton performance, and to reduce the amount of power required for cathode operation. Another secondary goal was to evaluate the performance of a bismuth cathode while operating with a bismuth Hall thruster.

5.3. Description of Apparatus

The cathode described here was designed to operate on bismuth as well as other typical propellants, such as xenon or krypton. A detailed schematic of the hybrid cathode can be seen in Figure 5-1. The overall dimensions of the cathode were 2.5 cm in diameter by 24 cm in length.

As shown at the top of Figure 5-1 a bismuth reservoir resides near the back of the cathode and is gravity-fed with hydrostatic pressure to a porous plug that separates the liquefied bismuth from the rest of the cathode. The cathode body is also equipped with a gas inlet line to allow it to operate on xenon or krypton. Inline with the gas inlet is a propellant line isolator (not shown) followed by a solenoid valve. The valve is closed when running on bismuth to prevent any escape of bismuth vapor back through the propellant line. Towards the front of the cathode is a LaB_6 emitter held in place by a tungsten spring as well as a molybdenum LaB_6 pellet holder. The cathode body was fabricated with titanium and has an end orifice of 2.0 mm. The bismuth and gas inlet were fabricated using 304 stainless steel. As shown in the schematic, there are two separate resistive heaters for the bismuth reservoir and the LaB_6 pellet. Three thermocouples were placed along the outside body of the cathode so that the temperature could be monitored and controlled for both the bismuth reservoir and the cathode body. The cathode was operated with both a tungsten keeper and an 8.9-cm-diameter, 17.8-cm-long cylindrical stainless steel anode (see Figure 5-2).

All of the testing reported here was performed in the Bismuth Test Facility at Michigan Technological University's Ion Space Propulsion Lab. Research was performed in a 2-meter-diameter by 4-meter-long vacuum chamber. The tank was evacuated using three magnetically levitated turbo-molecular pumps capable of pumping at 2000 L/s each and backed by a

mechanical pump with a pumping capacity of 400 ft^3/min. Using this facility, vacuum pressure of 10^{-6} Torr can be achieved in less than 50 minutes.

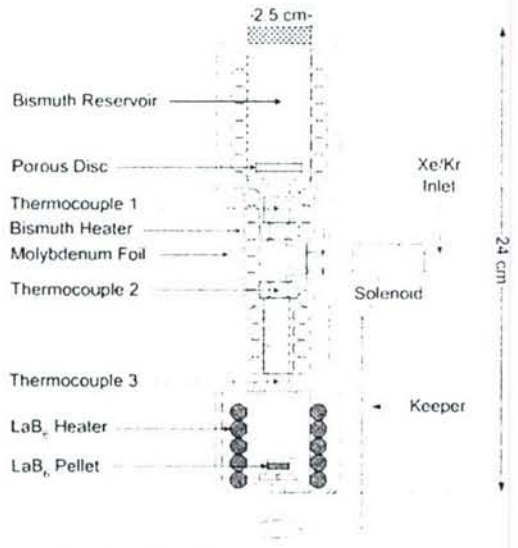


Figure 5-1. Bismuth cathode schematic and thermocouple placement.

5.4. Results

The cathode was conditioned by initiating a flow of krypton at 10 SCCM to the cathode and supplying approximately 275 watts of power to the LaB_6 heater. During this time the keeper was biased to 300 volts until discharge occurred. At this point the propellant flow was reduced to 3 SCCM and the keeper was current-limited at 4 amps. At 4 amps the keeper operated at approximately 38 volts. The LaB_6 heater power was then reduced to 90 watts and the bismuth reservoir heater was enabled and raised to a temperature at which the cathode could sustain solely on bismuth. To do this took 160 watts to the bismuth reservoir heater and 30 minutes. The gas flow was then terminated by closing the solenoid valve. The discharge was attached to the cylindrical anode at which point the data were taken. For each test the heater power remained constant throughout the duration of data collection so that the cathode could reach an equilibrium temperature. An electrical diagram of the cathode can be seen in Figure 5-2.

As mentioned, for all of the data reported here it was necessary to "jumpstart" the bismuth cathode using krypton. However, further testing was done with a similar cathode design where discharge was achieved using bismuth as the sole propellant. The two main downfalls that were experienced when solely using bismuth were that much more LaB_6 heater power was needed to obtain a discharge and once discharge occurred it was extremely difficult to keep the cathode operating stably.

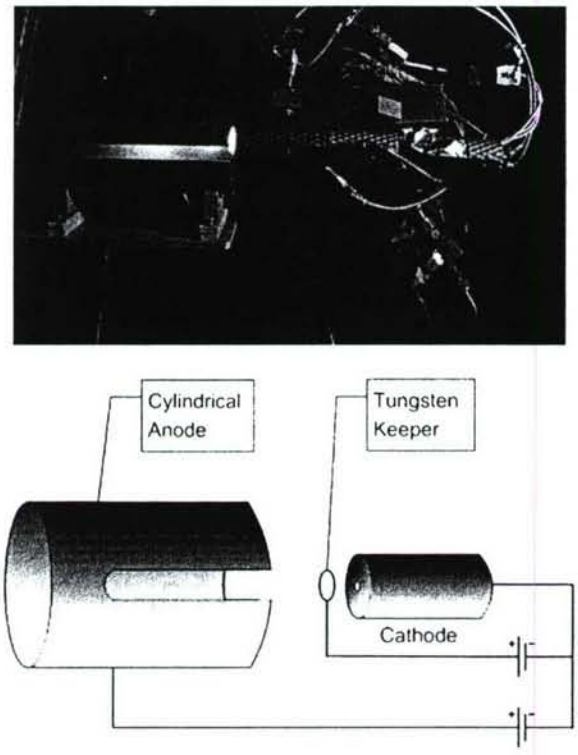


Figure 5-2. Operating bismuth cathode (top) and electrical schematic (bottom).

5.4.1. Bismuth Operation

The cathode mass was recorded pretest and posttest to determine a time-average rate of propellant mass flow. For this particular experiment the cathode mass flow rate was 0.71 ±0.03 mg/sec of bismuth. The temperature data recorded throughout the duration of the test from the three thermocouples shown in Figure 5-1 can be seen in Figure 5-3. As shown, for the first 30 minutes the cathode was operated using krypton. The cathode then operated only on bismuth for the rest of the test. Figure 5-4 shows multiple sets of voltage data taken over the 106-minute bismuth run time while sweeping from 2 to 16 amps in current-limited mode on the cylindrical anode.

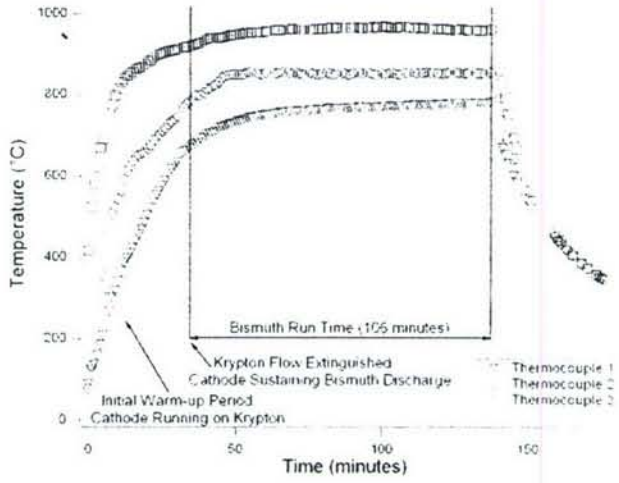


Figure 5-3. Temperature data taken near the bismuth reservoir, the cathode center, and the end orifice by thermocouples 1, 2, and 3, respectively, throughout the duration of the bismuth cathode test.

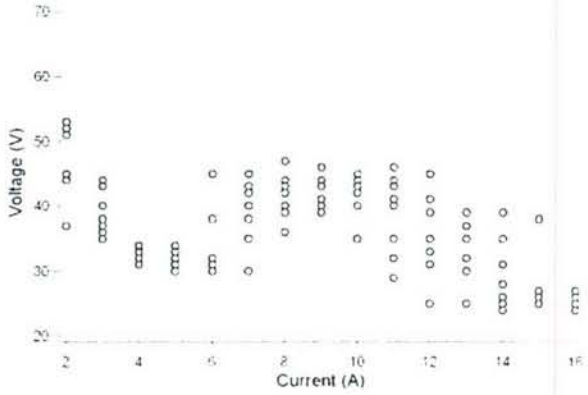


Figure 5-4. Anode voltage taken at currents varying from 2 to 16 Amps at a mass flow rate of 0.71 mg/s using bismuth.

5.4.2. Comparison with Xenon and Krypton

A cathode identical to the device used for bismuth characterization was then tested at two different xenon flow rates using a new LaB_6 emitter. The rates were chosen so that the same mass flow was used as in the bismuth case as well as the same molar flow. The equivalent molar flow rate for xenon is 0.45 mg/s. Three sweeps at each flow rate were taken and the results can be seen in Figure 5. The same experiment performed with xenon was then done using krypton. The identical cathode was used for krypton experimentation, including the LaB_6 emitter. The corresponding molar flow rate for krypton is 0.29 mg/s. These results can be found in Figure 5-5 as well.

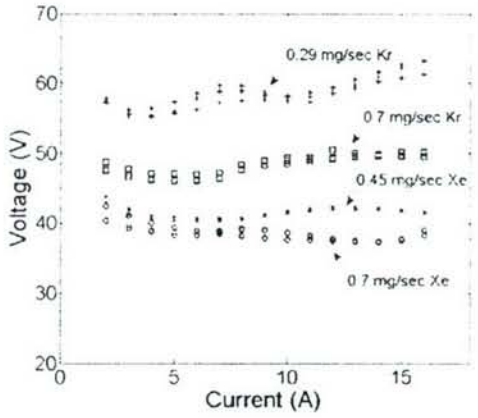


Figure 5-5. Anode voltage taken at currents varying from 2 to 16 amps using krypton and xenon propellants.

5.5. Discussion

5.5.1. Required Heater Power

The total heater power required for steady-state operation of the bismuth cathode was 250 watts. Approximately 160 watts were necessary for the bismuth reservoir and 90 were input into the LaB_6 heater. Further testing (not reported here) with the cathode on a 2-kW bismuth Hall thruster illustrated that the LaB_6 heater was unnecessary and that the cathode could operate on only 125 watts input to the bismuth reservoir heater. It should be noted that in each successive bismuth cathode experiment the LaB_6 heater power had to be increased to begin a discharge. Over a testing period of two weeks, the necessary power to light the cathode each consecutive time was 220, 240, 240, and 300 watts for the final test. It is interesting that a similar phenomenon was observed with a mercury hollow cathode using a 2% thoriated tungsten emitter. It was determined by Rawlin that the downstream end of the emitter was lacking emissive material, which made it necessary to increase heater power in further testing.[2] The increased degradation of emissive materials may be an artifact of using a metal vapor propellant as opposed to an inert gas.

5.5.2. I-V Characteristics

When using bismuth propellant, the range of anode voltages recorded was found to be between approximately 25 and 50 volts. This is comparable to the voltage range of 35 to 50 volts obtained from xenon and krypton, with the exception of the lowest flow rate, 0.29 mg/s, of krypton. At this particular flow rate the anode voltage was higher and ranged between 55 and 65 volts.

The xenon data of Figure 5-5 displays a variation in anode voltage of only 8% at 0.45 mg/s and 12% at 0.7 mg/s while the current was adjusted from 2 to 16 A. When operating using krypton propellant, the variation in anode voltage was 9% at 0.7 mg/s and 13% at 0.29 mg/s. The bismuth data in Figure 4 has a much large variation. The anode voltage varied as much as 57% over the discharge current sweep from 2 to 16 A. As the anode current is swept from 2 to 16 amps, the anode voltage has an overall decrease. Typically, voltage decreases are associated with mass flow increases for similar cathodes.[3,4] One hypothesis for this phenomenon is that increased cathode current caused localized heating near the orifice which then increased the mass flow rate, since the evaporative mass flow of bismuth is entirely temperature dependant.

5.5.3. Mass flow analysis

Researchers attempted to control the Bi evaporation rate by controlling the temperature of the reservoir. Equation 5-1 is a curve-fit for bismuth vapor pressure that when inserted into Equation 5-2, provides a gas kinetic estimate of mass flow per unit orifice area as a function of bismuth liquid temperature.[5] Note that S.I. units are used in both Equations 5-1 and 5-2.

$$P_v = \log^{-1}\left[13.317 - \frac{10114}{T} - 0.86\log T\right] \qquad 5\text{-}1$$

$$\frac{\dot{m}}{A} = \frac{P_v}{\sqrt{\frac{2\pi kT}{m}}} \qquad 5\text{-}2$$

Figure 5-6 is a plot of the mass flow rate per evaporation area at internal temperatures ranging from 700 to 1000°C. Assuming that the crucial temperature for bismuth flow is that of the cathode orifice, than it would have to maintain a temperature between 850 and 855°C to yield a flow rate of 0.71 mg/sec through the 2.0-mm-diameter orifice. However, taking sweeps of discharge current from 2 to 16 amps would cause large instantaneous changes in the temperature at the cathode end orifice. The increase in temperature would cause an increase in mass flow, which is what appears to be happening when the anode is given greater than 8 amps of discharge current.

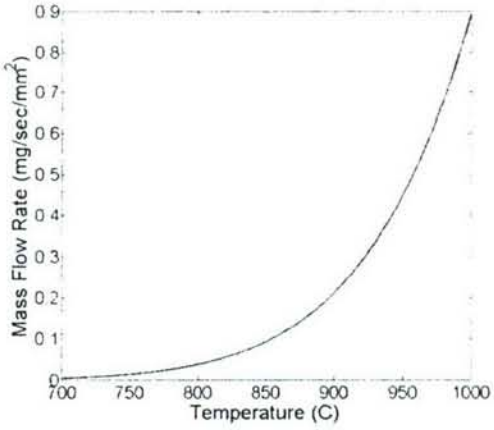


Figure 5-6. Bismuth evaporation rate per surface area as a function of temperature.

The thermocouple nearest the LaB_6, thermocouple 3 in Figure 5-1, read 960 ±10°C throughout the test. At this temperature the cathode would have a mass flow rate of 1.7 mg/s based on the end orifice area. Thermocouple 1 read 760 ±15°C which would have a mass flow rate of about 6.8 mg/s based on the porous vapor escape area. Prior to this investigation it was assumed that the governing temperature for bismuth flow rate would be at the porous disk. After operating the cathode numerous times using bismuth propellant it seems more likely that the most critical flow-limiting region is at the end orifice of the cathode. It is possible that the rate of evaporation from the porous disk is greater than that of the end orifice and that bismuth is condensing and accumulating within the cathode. The accumulated bismuth could then account for the transient periods of increased mass flow when the orifice region experienced localized heating at high discharge current.

5.6. Conclusions

A versatile LaB_6 cathode assembly was tested using bismuth, xenon, and krypton as propellant. For bismuth operation it was necessary to start the discharge on krypton and then switch to bismuth. It was demonstrated that 250 watts of power was sufficient for the bismuth cathode to sustain a stable discharge. Anode voltages were then recorded while sweeping the discharge current from 2 to 16 amps at a bismuth mass flow rate of 0.71 mg/s. The variation of anode voltage for the data set was about 57%.

For comparison, data was then taken using an identical cathode with a new LaB_6 emitter. Experiments were done with this cathode operating using both krypton and xenon propellants. Discharge current was swept between 2 and 16 amps and the anode voltages were recorded. The variation in anode voltage between all of the krypton and xenon data that were taken had a maximum of 13%.

To account for the difference between the bismuth, xenon, and krypton trends it was determined that an increase in discharge power may have an effect on the amount of bismuth being evaporated from the end orifice. It is evident that the most critical temperature for mass flow control is at the end orifice rather than the porous stainless disk. However, control of the porous disk temperature is also crucial since it must be hot enough to allow for sufficient bismuth evaporation to the orifice region.

---

[1] Makela, J.M., King, L.B., Massey, D.R., and Fossum, E.C., "Development and Testing of a Prototype Bismuth Cathode for Hall Thrusters," AIAA-2005-4236, 41st AIAA/ASME/SAE/ASEE Joint Propulsion Conference, July 10-14, Tucson, AZ.

[2] Rawlin, V.K., "A 13,000 Hour Test of a Mercury Hollow Cathode," Nasa Technical Memorandum, Nasa TM X-2785. June 1973, Washington, D.C.

[3] Domonkos, MT, "Evaluation of Low-Current Orificed Hollow Cathodes", Ph.D. Dissertation, University of Michigan, 1999

[4] Goebel, D.M, and Watkins, R.M., "LaB_6 Cathodes for Ion and Hall Thrusters," AIAA 2005-4239, 41st Joint Propulsion Conference, Tucson, AZ.

[5] Gray, D.E. ed., American Institute of Physics Handbook 3rd Edition, McGraw-Hill, 1972.